Journal of Nanobiotechnology

RESEARCH Open Access

Astragaloside IV- loaded biomimetic nanoparticles target IκBα to regulate neutrophil extracellular trap formation for sepsis therapy

Shujuan Wu[1,2†], Mengqi Zhou[3†], Huimin Zhou[1†], Lu Han[3] and Huifan Liu[1*]

Abstract
This study explored the novel mechanism of Astragaloside IV (As) in treating sepsis and its application through a biomimetic nano-delivery system (As@ZM). Sepsis, a condition of organ dysfunction caused by an abnormal host response to infection, poses a significant threat to global health due to its high mortality rate. Our findings revealed a new mechanism for As in treating sepsis, which involved the reduction of neutrophil extracellular traps (NETs) release, potentially related to As binding with IκBα to inhibit the activation of the NF-κB pathway. As treated neutrophils also improved the immune microenvironment by crosstalk with endothelial cells and lung epithelial cells. However, the stability and bioavailability of As limited its clinical application. To address this issue, we had developed a ZIF-8-based nano-delivery system that achieved targeted delivery through neutrophil membrane coating, significantly enhancing the therapeutic efficacy of As. The innovative design of As@ZM offered a new strategy for sepsis treatment, with the potential to improve clinical outcomes.

Introduction

Sepsis is defined as a life-threatening dysfunction of organs, including the lung, liver, kidney, and brain, caused by the host's dysfunctional response to infection, and is characterized by inflammatory cytokine storms [1]. The mortality rate of hospitalized patients with sepsis has been reported to be up to 30–45% [2], making it a major threat to global health. Despite the deepening of sepsis associated research, there is still a lack of effective targeted treatment strategies. Neutrophils are the most abundant white blood cells in mammals and play a key role in the pathogenesis of sepsis [3]. As the first line of innate immune defense against infection, in addition to traditional mechanisms such as phagocytosis or the release of antibacterial substances such as inflammatory cytokines and reactive oxygen species, activated neutrophils also release a network structure composed of entangled densified DNA, histone, myelopperoxidase and other particles, called neutrophils extracellular traps (NETs), which can effectively trap circulating bacteria [4, 5]. However, excessive neutrophil activation and NETs release through damage-associated molecular patterns (DAMP) aggravate the inflammatory response of the body [6], inhibit the normal proliferation of endothelial cells and histiocytes, increase endothelial permeability, cause microcirculation impairment, and eventually lead to multiple organ injury and failure [3]. Silva et al.

†Shujuan Wu, Mengqi Zhou and Huimin Zhou authors contributed equally to this work

*Correspondence:
Huifan Liu
huifan@whu.edu.cn

Full list of author information is available at the end of the article

Graphical abstract

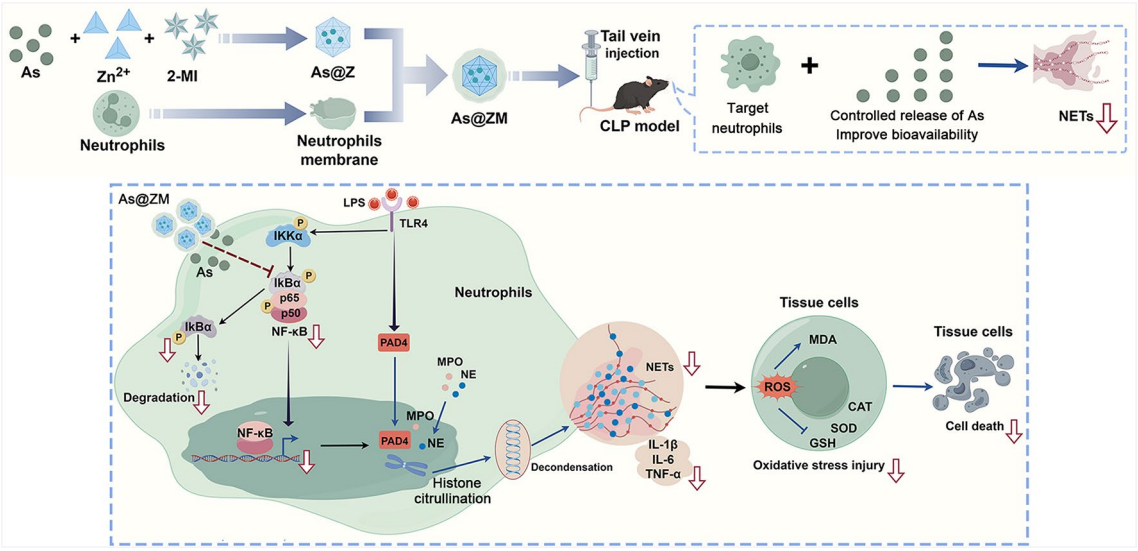

Keywords Sepsis, Astragaloside IV, Neutrophil extracellular traps, NF-κB, Biomimetic nanoparticle

demonstrated that the elimination of NETs formation with disulfiram was effective in reducing mortality from multiple organ dysfunction and sepsis [7].

Astragaloside IV (As) is a small molecule saponin extracted from Astragaloside root, one of the important effective components, with outstanding antioxidant, anti-inflammatory, anti-apoptotic and immune regulation effects [8]. Its main mechanisms include negative regulation of Gpr97-TPL2 signaling [9], regulation of Nrf2 [10], MAPK [8], TGF-β [11], NF-κB [12] signaling pathways, etc. As a classical inflammatory pathway, NF-κB pathway is closely related to NETs. Inhibition of NF-κB activation with pyrrolidine dithiocarbamate significantly reduced the formation of NETs in renal tissue [13]. However, the relationship between As and NETs is unclear. Here, we found that the novel mechanism of As in the treatment of organ damage in sepsis was to reduce the release of NETs, which might be related to the inhibition of the activation of NF-κB pathway by As binding to IκBα. Meanwhile, As alleviated death and oxidative stress of endothelial cells and lung epithelial cells by treating neutrophils.

Despite the broad clinical application prospects of As in the treatment of sepsis, its practical use is hindered by factors such as poor stability and insufficient bioavailability [14, 15]. To overcome these limitations, we have designed and developed a biomimetic nanodelivery system to achieve targeted delivery and controlled release of As. In the field of nanodrug delivery systems, we observe that there are various nanocarriers to choose from, including PLGA, MSNP, and Fe_3O_4, among others. These nanocarriers all exhibit high drug-loading capacities. However, Zeolitic Imidazolate Framework-8 (ZIF-8) demonstrates advantages in drug delivery due to its unique porous structure. It can achieve high drug loading and controlled release, thereby enhancing efficacy and reducing side effects. Furthermore, ZIF-8 shows excellent biocompatibility and stability, protecting drugs from degradation. The tunable pore size and surface chemistry of ZIF-8 allow for optimization of the drug delivery process, supporting personalized medicine. Additionally, ZIF-8 can improve the bioavailability of poorly soluble drugs. These characteristics make ZIF-8 a prominent candidate material for advanced drug delivery systems, especially in the field of nanomedicine [16]. ZIF-8, a branch of metal-organic frameworks (MOFs), is rapidly self-assembled from zinc ions (Zn^{2+}) and 2-methylimidazole (2-MI) [17]. By encapsulating As within ZIF-8 nanoparticles (referred to as As@Z), we aim to prevent the rapid degradation and elimination of As in the bloodstream, while enhancing its stability and bioavailability. To improve the targeting to neutrophils, we used the neutrophil membrane as the outer coating of As@Z nanoparticles, thus preparing a new type of biomimetic nanoparticle (referred to as As@ZM). Our further research has confirmed that this new type of biomimetic nanoparticle As@ZM significantly enhances the efficacy of As, providing a new strategy for the treatment of sepsis.

Materials and methods

Materials

As and lipopolysaccharide (LPS) were purchased from MedChemExpress (Monmouth Junction, NJ, USA). Zinc

nitrate hexahydrate [$Zn(NO_3)_2{\cdot}6H_2O$] and 2-methylimidazole (2-MI) were purchased from Aladdin Biochemical Technology Co., LTD (Shanghai, China). For in vitro cell culture, fetal bovine serum (FBS), RPMI 1640, DMEM, DMEM/F12 medium, PBS, trypsin-EDTA, and penicillin/streptomycin (P/S) were purchased from Cytiva Biotechnology Co., Ltd (Washington, USA). The MLE-12, HL60, and HUVEC cell line was provided by Wuhan Pricella Biotechnology Co., Ltd (Wuhan, China). A Cell Counting Kit-8 (CCK-8) kit was purchased from Dojindo Laboratories (Kumamoto, Japan), while a live/dead cell staining kit was obtained from Baxter Biotechnology (Shanghai, China). Triton X-100 and DAPI for cell staining were sourced from Sigma–Aldrich. The radioimmunoprecipitation lysis buffer (RIPA), and bicinchoninic acid (BCA) protein detection kit were purchased from Jiangsu Beitian Biotechnology Co., Ltd. All chemicals used in the study were not further purified.

Cell culture

Mouse peripheral blood neutrophils (PBNs) were collected from the whole blood of C57BL/6 mice (8 weeks old, male) by using a mouse peripheral blood neutrophil separator kit (Solarbio, Beijing, China). The mice were anesthetized, and their blood was collected into anticoagulation tubes by apex cordis bleeding. Within one hours, the blood was diluted twice and added carefully to the prepared separation system. The samples were centrifuged at 1500 × g for 30 min at 25 °C, and then the neutrophils were separated at the boundary between the different interfaces and transferred carefully to a clean centrifuge tube. To remove the undesired erythrocytes, a sufficient amount of lysis buffer was added to the tube. Neutrophils were washed with PBS three times, and were suspended in Mouse peripheral blood neutrophils complete culture medium (CP-M150, Pricella, Wuhan, China).

The HL-60 cells were cultured in RPMI 1640 complete media and treated with 1.3% DMSO for 6 to 7 days for differentiation to dHL-60 cells. The MLE12 cell line was cultured in DMEM/F12 medium, and the HUVEC cell line was cultured in DMEM medium. All cell cultures were supplemented with 10% FBS (Gibco) and 1% Penicillin-Streptomycin Solution (Biosharp), and incubated at 37 °C in a 5% CO_2 atmosphere.

Patients and specimens from patients with clinical sepsis

Patients diagnosed with sepsis according to Sepsis 3.0 were recruited for this study based on their own criteria. Human blood specimens were collected from 20 sepsis patients in the Department of Intensive Care Unit and 20 healthy volunteers at Renmin Hospital of Wuhan University between March 2023 and March 2024. Blood samples were obtained and prepared for enzyme-linked immunosorbent assay (ELISA) within a two-hour timeframe. The study protocol for sepsis patients was approved by the Medical Ethics Committee of Renmin Hospital, Wuhan University (WDRY2022-K046). Prior to inclusion in the study, written informed consent was obtained from all enrolled participants. The baseline data of patients were shown in Table S1.

Animal models

Specific pathogen-free (SPF) male C57BL/6 mice, aged 8–10 weeks, were sourced from Wuhan University (Wuhan, China). We established sepsis animal models using two technical approaches: cecal ligation and puncture (CLP) surgery, and intraperitoneal injection of LPS.

The CLP surgery: Anesthesia was induced via intraperitoneal injection of a combination of 75 mg/kg ketamine and 10 mg/kg xylazine. A midline incision was meticulously executed in the abdominal wall to gently extract the cecum, preserving the integrity of the mesenteric vasculature. The cecal apex was delicately manipulated by compressing its proximal end to distend its tip and isolate the mesenteric surface vasculature. Thereafter, sterile 4 – 0 silk suture was employed to ligate both the ileocecal valve and the cecal midpoint. A subsequent step involved piercing the cecum at the ligated sites and its apex using a sterile 21 G needle to create perforations. To ascertain patency of these perforations, a minute quantity of cecal contents was gently extruded, evacuated, and the cecum was repositioned within the abdominal cavity. The abdominal cavity was then closed and sutured, followed by a resuscitative regimen consisting of 50 mL/kg saline administration to each mouse. Postoperative management included analgesia with buprenorphine at a dose of 0.05 mg/kg. Another approach employed for establishing the sepsis animal model involved the intraperitoneal administration of LPS at a dose of 15 mg/kg to each mouse. All experiments conducted adhered strictly to National Institutes of Health (NIH) standards and received approval from Wuhan University's Animal Ethics Committee (Ethical Approval Number ZN2023186).

Conditioned medium (CM) collection

The culture medium of PBNs cells was collected after treatment or untreated with LPS and As. Subsequently, the medium was centrifuged at 2000 rpm for 10 min to pellet any cell debris, and the supernatant was transferred to sterile 15 mL centrifuge tubes. The collected CM samples were stored at -80 °C for subsequent ELISA detection and co-culture with MLE12 cells. For co-culture experiments, MLE12 cells were incubated with an equal volume mixture (1:1 ratio) of CM and fresh medium for 24 h. The same procedure was used to collect dHL-60 cell culture medium for co-culture with HUVEC cells.

Preparation of the ZIF-8, As@Z, and As@ZM nanomaterials

The synthesis of As@Z was carried out using a simple one-pot method. Specifically, 0.41 g 2-MI and 20 mg As were dissolved in 2 mL ddH_2O, followed by the rapid addition of 140 μL 0.5 M $Zn(NO_3)_2{\cdot}6H_2O$ solution to the mixture. The resulting colloid was stirred for 20 min at room temperature and then collected by centrifugation (10,000 r, 20 min), washed with ddH_2O three times, and redispersed in ddH_2O for further use.

A blank ZIF-8 was prepared using a similar procedure without the addition of As. Prior to preparing the As@ZM NPs, membrane fragments from PBNs were obtained using a plasma membrane protein separation kit. To prepare As@ZM, membrane fragments at a concentration of 1 mg/mL were mixed with As@Z at a concentration of 1 mg/mL in cold PBS. After undergoing ultrasonic treatment for five minutes, the resulting NPs were collected by centrifugation at 10,000 rpm for 20 min. The precipitate was washed with PBS three times and then redispersed in PBS for further use.

Characterization of the ZIF-8, As@Z, and As@ZM nanomaterials

The morphology of the synthesized nanomaterials was analyzed using transmission electron microscopy (TEM, JEM2100, Hitachi, Tokyo, Japan) and scanning electron microscopy (SEM, USA-FEI-NOVA NANOSEM 230). The particle size and zeta potential of the nanoparticles prepared in aqueous solution were measured using a NICOMP 380ZLS zeta potential/particle sizer (PSS NICOMP, Santa Barbara, California, USA). Thermogravimetric analysis (TGA) was conducted with a thermal analyzer (Diamond TG/DTA; PerkinElmer Instruments, Shanghai, China) at a heating rate of 10 °C min^{-1} from 30 to 900 °C under nitrogen flow. SDS-PAGE was performed to separate the proteins. The protein concentration was determined using a BCA kit. Equal volumes of protein samples were loaded onto a 10% SDS–PAGE gel after being mixed with buffer and heated at 95 °C for 5 min. Following decolorization with water, the proteins were stained with Coomassie brilliant blue and imaged overnight.

Encapsulation efficiency, drug loading capacity, and drug release behavior

The As content was quantified using high-performance liquid chromatography (HPLC, Agilent, USA) at a wavelength of 203 nm. Free As was removed through ultrafiltration with a molecular weight cut-off value of 10 kDa. The encapsulation efficiency and drug loading capacity of the nanoparticles were determined as follows: encapsulation efficiency (%) = amount of encapsulated As/the amount of added As ×100%; drug loading capacity (%) = amount of encapsulated As/the total amount of nanoparticles ×100%.

The release of As in vitro was investigated using PBS as a sustained release medium. Briefly, 2 mg nanoparticles were placed in a dialysis bag with 1 mL PBS (pH 7.4) and immersed in a centrifuge tube containing 15 mL PBS solution (pH 7.4). The drug release experiment was conducted at 37 °C with a frequency of 100 r/min. At predetermined time intervals, 1 mL samples were collected to determine the amount of As released from the nanoparticles. To maintain a constant volume, the collected sample (1 mL) was returned to the centrifuge tube along with fresh PBS solution.

The cumulative release percentage (CR%) of As was calculated using the following formula: $CR\% = [(V_0 \times C_t + V \times CR\% = [(V_0 \times C_t + V\times)/M_{total} \times 100\%])/M_{total} \times 100\%]$, where V_0 represented the initial diluent volume, C_t represented the concentration of As at time t, V represented the volume of sample taken out, C represented its corresponding concentration, and M_{total} was the total mass of loaded As in the nanoparticles.

Cytocompatibility biocompatibility assay for As@ZM

A hemolysis experiment was conducted to assess the hemocompatibility of the different nanoparticle samples following coculture. The experimental procedure was as follows: 1 mL fresh C57BL/6 mouse anticoagulated whole blood was diluted with 1.25 mL normal saline to obtain a homogeneous suspension. The various groups of nanoparticles were added to 10 mL normal saline, preheated at 37 °C for 30 min, and then mixed gently with 0.2 mL diluted blood sample. After incubation at 37 °C for 1 h, all the mixed solutions were centrifuged at 3000 rpm for 15 min to precipitate complete red blood cells. Subsequently, 1 mL the supernatant was carefully transferred into new tubes, after which the absorbance was measured at a wavelength of 540 nm using a UV-Vis spectrophotometer (Perkin Elmer, USA). The negative and positive controls consisted of normal saline and DI water, respectively. The formula used to calculate the hemolysis rate was as follows: hemolysis rate (%)=(A1-A0)/(A2-A0)×100%, where A1, A0, and A2 represented the absorbance values obtained from the supernatants in the experimental group, negative control group, and positive control group, respectively. In vivo, healthy C57BL/6 mice ($n = 5$) were administered NPs (30 mg/kg) via the tail vein. After 2 weeks, the organs (heart, liver, spleen, lung, and kidney) were collected, fixed with formalin, stained with H&E, and pathologically analysed.

Western blotting analysis

Total protein was extracted using the RIPA Protein Lysis Buffer (Biosharp) supplemented with protease and phosphatase inhibitors (MedChemExpress, MCE). The

nuclear protein was extracted with the Nuclear and Cytoplasmic Protein Extraction kit according to the instructions (Beyotime). BCA Protein Assay Kit (Beyotime) was used to determine protein concentrations. The proteins were resolved by 10% SDS-PAGE and subsequently transferred onto polyvinylidene fluoride (PVDF) membranes. Membranes were incubated with specific primary antibodies at 4 °C overnight. The next day, after washing with Tris-Buffered Saline with Tween 20 (TBST) for 5 min five times, membranes were incubated with horseradish peroxidase (HRP)-conjugated secondary antibodies (1:5000 dilution; ABclonal) for 1 h at room temperature. The primary antibodies used in this study was provided in Table S2. Following the secondary antibody incubation, the membranes were washed again with TBST. The blot images were then captured using the Bio-Rad Chemi-Doc™ XRS + System or Roche with a highly sensitive ECL luminescent solution (Biosharp). The gray values of the blots were quantified using ImageJ software.

ELISA

The levels of IL-6, IL-1β, TNF-α were determined by ELISA kits (ABclonal, Shanghai, China) for human or mouse. Each sample was measured in duplicate.

Target prediction and molecular Docking

The molecular structure of As was downloaded from the PUBCHEM database. The target genes of As were then retrieved using SuperPred and SwissTargetPrediction databases. "Sepsis" was used as a keyword to predict the target genes associated with sepsis by the OMIM, GeneCards and CTD databases and dataset GSE54514, and then analyzed emoplying the jvenn tool. Following this, a Venn diagram analysis using jvenn was conducted to identify the overlapping genes between the predicted target genes of As and the sepsis-related genes. Gene symbol of 31 target genes with intersection was imported into the String (https://string-db.org/) service platform, and the limited species was Homo sapiens to construct a protein–protein interaction (PPI) network. The PPI network was visualized by Cytoscape 3.10.1 software and the top 7 Hub target genes were obtained.

Molecular docking was performed between IκBα and As. Protein preparation, including dehydrogenation, removal of water molecules, and elimination of non-ligand small molecules, was carried out using PyMol 2.5.5 software. Subsequently, a docking box was defined to enclose the protein's active site. ADFRsuite 1.0 was then used to convert the small molecules and receptor proteins from PDB to PDBQT format. The docking process was executed, and the conformation exhibiting the highest affinity score was chosen as the correct one. Finally, visual analysis was conducted using PyMol 2.5.5 to inspect the docking results.

DCFH-DA detection

For reactive oxygen species (ROS) measurement, cells were loaded with DCFH-DA, a fluorescent probe for ROS (Beyotime) at 10 μM in each well of a six-well plate. After further culture for 30 min in the dark, the cells were detected by flow cytometry.

GSH, SOD, CAT and MDA detection

The GSH (Nanjing Jiancheng, A006-2-1), SOD (Nanjing Jiancheng, A001-3-2), CAT (Nanjing Jiancheng, A007-1-1) and MDA (Nanjing Jiancheng, A003-1-2) concentrations in MLE12 cells were detected according to manufacturer's instructions.

Cellular thermal shift assay (CETSA)

PBNs or dHL60 were lysed on ice using RIPA lysis buffer for 40 min, followed by centrifugation at 12,000 g at 4 °C to collect the supernatant. Subsequently, the cell lysed were incubated with either 20 ug/mL As or DMSO for 3 h at room temperature. The resulting lysate was divided into microtubes (50 μL) and subjected to heating at the specified temperature range (37–62 °C) for 5 min. After heating, the microtubes were immediately placed on ice for a duration of 5 min. Then, collecting supernatant through centrifugation at 12,000 g at 4 °C for 10 min and supplemented with SDS protein loading buffer before being boiled at 95 °C for an additional period of 5 min in preparation for Western blotting.

Statistical analysis

All data were analyzed with the GraphPad Prism 8 software. All quantitative data were presented as mean ± standard deviation (SD). Multiple comparisons were used by one-way ANOVA, followed by Tukey's post-hoc test. All the p-values were shown in the figures, and $p < 0.05$ was considered statistically significant.

Results

Regulating NETs levels might emerge as a novel therapeutic approach for sepsis

At the clinical level, this study enrolled patients diagnosed with sepsis in accordance with Sepsis 3.0 criteria, as well as healthy volunteers. The detection results showed that the levels of CitH3-DNA and MPO-DNA complexes, which were specific biomarkers of NETs, were significantly elevated in the peripheral blood of septic patients (Fig. 1A-B). Concurrently, the levels of inflammatory cytokines IL-1β and TNF-α were also significantly increased in the peripheral blood of septic patients (Fig. 1C-D). Moreover, there was a significant correlation between NET biomarkers and inflammatory cytokines (Fig. 1E-H). Further research had revealed a significant correlation between the increase in NETs levels and the elevation of SOFA scores as well as APACHE

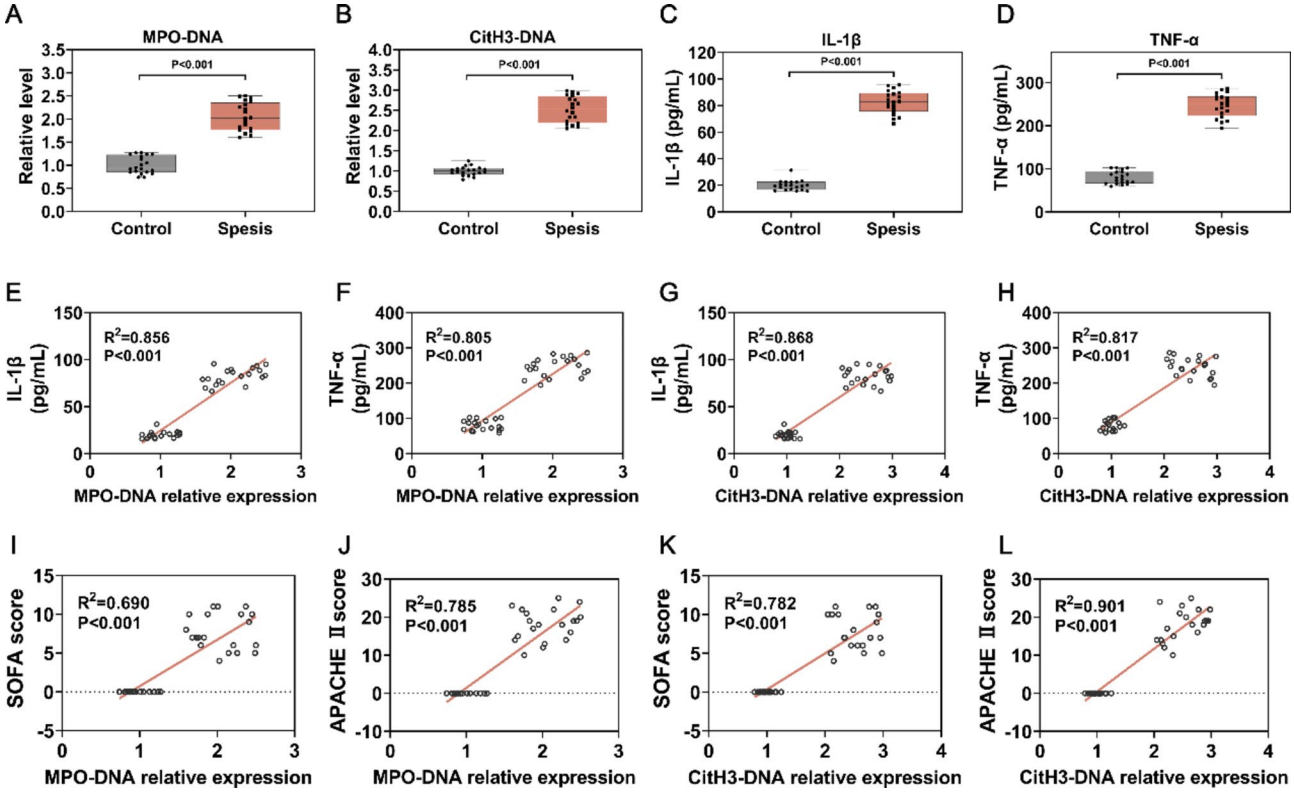

Fig. 1 NETs and inflammatory factors in peripheral blood were increased in patients with sepsis. (**A-B**) The MPO-DNA and CitH3-DNA concentrations in the plasma from control and patients with sepsis were determined ($n = 20$). (**C-D**) ELISA to detect the concentations of cytokine IL-1β and TNF-α in control and sepsis group ($n = 20$). (**E-H**) Pearson correlation analysis of IL-1β, TNF-α and MPO-DNA and CitH3-DNA, respectively. (**I-L**) Pearson correlation analysis of SOFA, APACHE II score and MPO-DNA and CitH3-DNA, respectively. All the data in A-D are presented as the mean ± SD. $P < 0.05$ indicate significant differences

II scores (Fig. 1I-L). Therefore, based on the aforementioned results, we could conclude that there was a close correlation between neutrophil extracellular traps levels and sepsis. Consequently, regulating the levels of NETs may represent a novel therapeutic strategy for the treatment of sepsis.

Astragaloside IV achieved significant protective effects for both CLP-induced and LPS-induced sepsis mice

In the quest to discover new drugs capable of modulating NETs levels for the treatment of sepsis, we have screened various bioactive components from traditional herbal medicines. Among these components, Astragaloside IV-As is a small molecular saponin extracted from the roots of Astragalus membranaceus, a key active constituent of the herb, renowned for its potent anti-inflammatory and anti-apoptotic properties. In subsequent experimental studies, As has demonstrated promising potential in regulating NETs and treating septic mice.

The structural formula of As is shown in Figure S1. To explore the potential role of As in the treatment of sepsis, we established two sepsis models: a bacterial sepsis model (induced by CLP) and endotoxemic shock model (induced by LPS). For the first 3 days before model establishment, we administered the drug to mice once daily via intraperitoneal injection at a dose of 20 mg/kg. After model establishment, we collected peripheral blood samples from mice at 12 h and tissue samples from lung, liver, and kidney at 24 h. We also continuously monitored the survival status of mice and plotted a 7-day survival curve (Fig. 2A). To determine the optimal therapeutic dose of As, we conducted an in vivo study with dose gradients ranging from 0 to 40 mg/kg. Through H&E staining and lung injury scoring, we observed significant pathological damage in lung tissues of CLP model mice including bleeding, edema, inflammatory cell infiltration, and tissue disorganization. After treatment with As, these injuries were alleviated to some extent, especially in the group treated with a dose of 20 mg/kg where lung injury improvement was most significant (Fig. 2B-C). Afterwards, we further investigated the therapeutic effect of As on sepsis using a dose of 20 mg/kg. Firstly, in the CLP model mice, we analyzed and plotted the 7-day survival curve. The results showed that the 7-day survival rate of mice in the CLP + Mock group was 35.0% (7/20), while it was 50.0% (10/20) in the CLP + As group, indicating that As treatment improved the 7-day survival rate of CLP mice (Fig. 2D). Next, to explore the effect

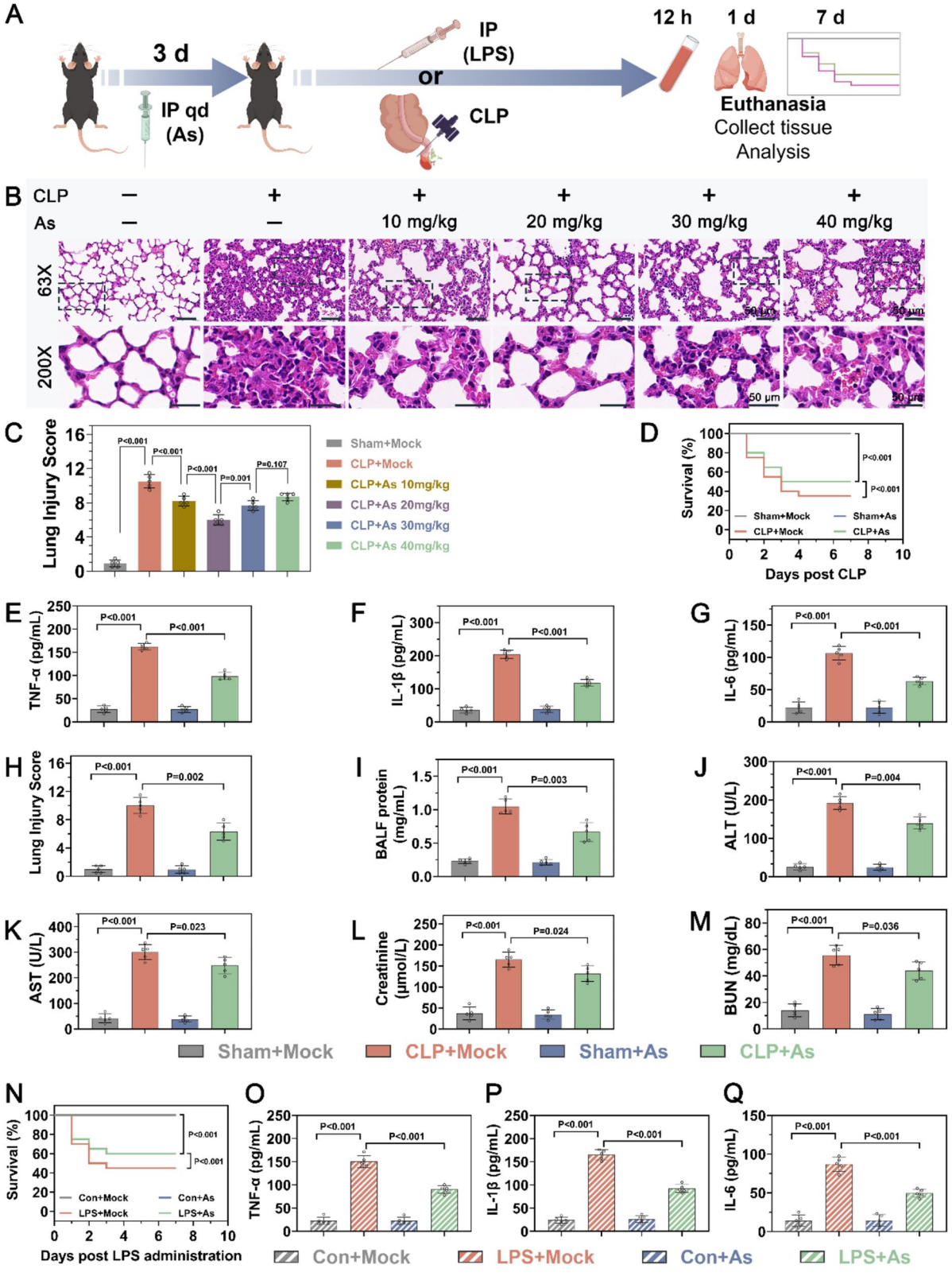

Fig. 2 (See legend on next page.)

(See figure on previous page.)

Fig. 2 Astragaloside alleviated the damage of important target organs in septic mice. (**A**) Schematic representation of the animal experimental in which Astragaloside was IP injected 3 days before the mice were subjected to CLP or LPS IP injection and the animals were euthanized after 12 h, 1 days or 7 days. (**B**) H&E staining to observe the pathological structure of lung tissue in CLP mice treated with different concentrations of As. The box showed a 200X magnification of the location ($n=5$). Scale bars = 50 μm. (**C**) Smith score of lung tissue to determine the optimal acting concentration of As ($n=5$). (**D**) Survival curves of mice in different treatment groups ($n=20$). (**E-G**) ELISA was used to detect the levels of the TNF-α, IL-1β and IL-6 in the plasma of mice in Sham + Mock, Sham + As, CLP + Mock and CLP + As groups ($n=5$). (**H-I**) lung injury index Smith score and BALF protein concentration and (**J-K**) liver injury index ALT and AST concentrations and (**L-M**) kidney injury index creatine and BUN concentrations in the plasma from mice in Sham + Mock, Sham + As, CLP + Mock and CLP + As groups were determined ($n=5$). (**N**) Survival curves of mice in Con + Mock, Con + As, LPS + Mock and LPS + As groups ($n=20$). (**O-Q**) ELISA was used to detect the levels of the TNF-α, IL-1β and IL-6 in the plasma of mice in Con + Mock, Con + As, LPS + Mock and LPS + As groups ($n=5$). The data are expressed as mean ± SD. $P<0.05$ indicate significant differences

of As treatment on systemic inflammatory response in CLP mice, we measured levels of inflammatory factors in peripheral blood using ELISA. The results showed that compared to the Sham + Mock group, levels of TNF-α, IL-1β and IL-6 were significantly elevated in the CLP + Mock group mice, while they were lower in the CLP + As group than in the CLP + Mock group, indicating that As treatment reduced levels of inflammatory factors in peripheral blood of CLP mice (Fig. 2E-G). To further investigate the effects of As treatment on the organ damage in CLP-induced septic mice, we utilized H&E staining and assessed the severity of lung injury in the mice by lung injury scoring and the protein concentration in bronchoalveolar lavage fluid (BALF) (Figure S2, Fig. 2H-I). Additionally, we measured the levels of ALT and AST through blood biochemical tests to evaluate the extent of liver injury (Fig. 2J-K). Similarly, the severity of kidney injury was assessed by determining the levels of creatinine and blood urea nitrogen (BUN) in the serum (Fig. 2L-M). The results showed that compared to Sham + Mock group, detailed lung injury scores as well as liver and kidney damage were aggravated in CLP + Mock group mice; whereas As treatment alleviated major organ damage severity in CLP mice (Fig. 2H-M). The same results were observed in LPS-induced mouse models (Fig. 2N-Q). Therefore, we concluded that As treatment not only improved the short-term survival rate of septic mice, but also effectively reduced their systemic inflammatory response and damage to major organs.

Astragaloside IV effectively reduced the high levels of NETs caused by sepsis

Following a comprehensive assessment of the therapeutic effects of As on sepsis, we intend to delve deeper into the underlying mechanisms of its potential treatment. In the study depicted in Fig. 1, we observed that the levels of NETs in the peripheral circulation of patients with sepsis were significantly higher than those in the healthy control group. Moreover, the levels of NETs were positively correlated with the intensity of the body's inflammatory response. This discovery underscores the pivotal role of NETs in the etiology and progression of sepsis. Building on this foundation, we plan to examine the impact of As on the levels of NETs in sepsis patients and explore the mechanisms behind its therapeutic action.

We labeled neutrophils with ly6G and used immunohistochemical staining to analyze the lung tissues of CLP mice, we observed a significant increase in neutrophil infiltration in the CLP + Mock group compared to the Sham + Mock group. In the CLP + As group of mice that received As treatment, the degree of this neutrophil infiltration was reduced (Fig. 3A-B). Subsequently, the levels of NETs biomarkers - CitH3-DNA complexes and MPO-DNA complexes in peripheral blood samples from CLP-induced septic mice were detected by ELISA. The results showed that As treatment effectively reduced the elevated levels of NETs induced by CLP (Fig. 3C-D). Additionally, a similar decrease effect was also observed in the LPS-induced sepsis model (Fig. 3E-F). Additionally, immunofluorescence results showed that compared with the Sham + Mock group, the fluorescence levels of CitH3 and MPO in the lung tissues of mice in the CLP + Mock group were significantly increased, while the fluorescence levels of CitH3 and MPO in the CLP + As group were reduced (Fig. 3G-I).

Synthesizing the aforementioned findings, we had thoroughly validated through in vivo experiments that As could reduce the levels of NETs in septic mice. However, to further confirm the effects of As, additional in vitro validation is required. To determine the optimal in vitro therapeutic dosage of As, we conducted in vitro studies using a range of concentrations, specifically a gradient of 0, 10, 20, 30, and 40 μg/mL. The study found that As at concentrations of 10 μg/mL and 20 μg/mL had no significant effect on the proliferation of MLE12 cells, while As at concentrations of 30 μg/mL and 40 μg/mL exhibited a certain inhibitory effect on the proliferation of MLE12 cells (Figure S3). Based on these findings, we selected the 20 μg/mL dosage of As to further explore its regulatory effect on NETs through in vitro experiments. We utilized two types of neutrophils (PBNs and dHL60), subjecting them to corresponding treatments. After 24 h, we collected the cell culture supernatants and conducted assays for inflammatory cytokines and NETs (Fig. 4A). The results indicated that under LPS stimulation, PBNs produced higher levels of inflammatory cytokines, including TNF-α, IL-1β and IL-6, while treatment with As reduced

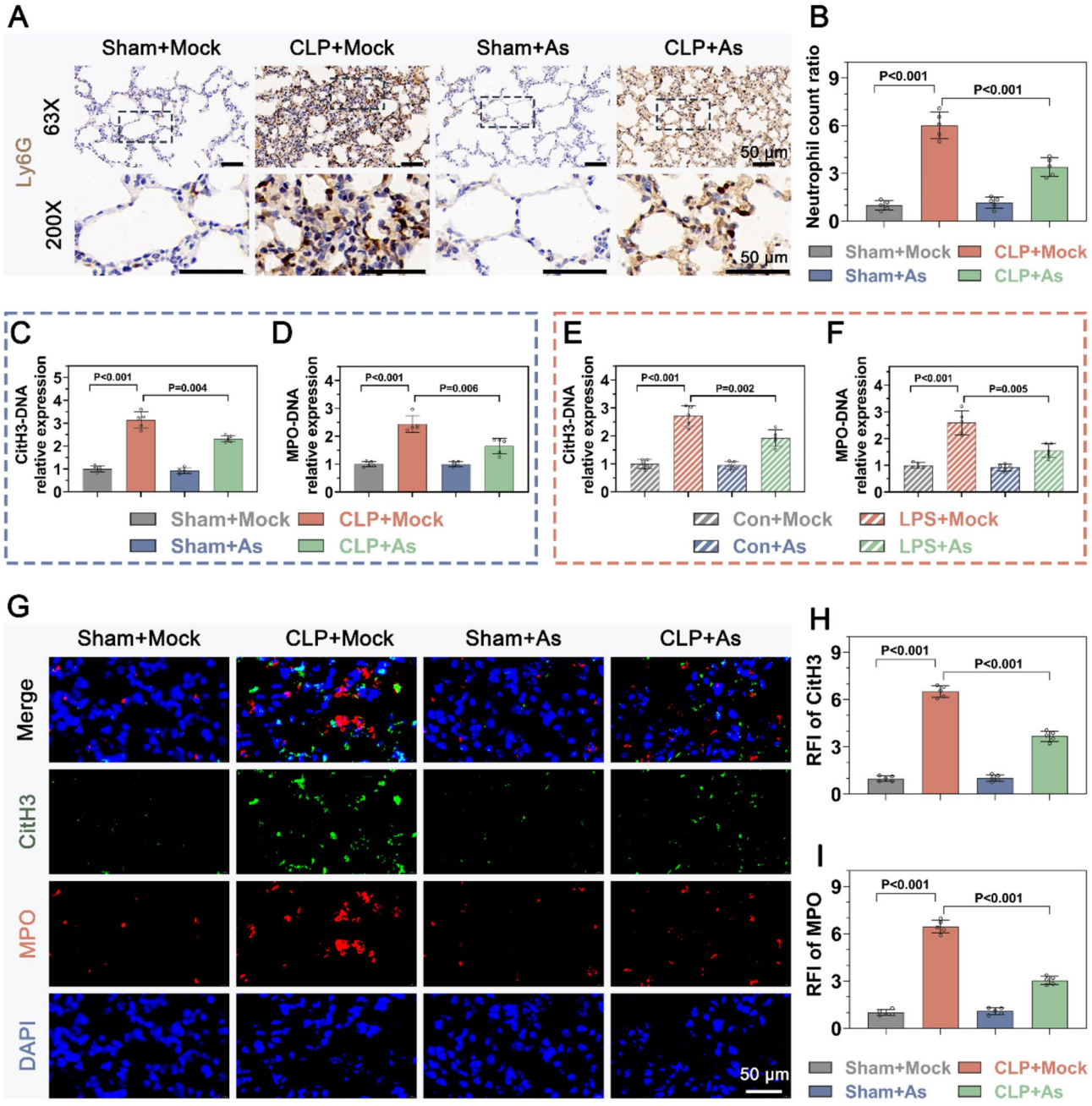

Fig. 3 Astragaloside alleviated NETs in mice with sepsis. (**A-B**) The number of neutrophils in lung tissue was detected by Ly6G immunohistochemistry in Sham + Mock, CLP + Mock, Sham + As and CLP + As groups. The box showed a 200X magnification of the location. Scale bars = 50 μm. (**C-F**) The MPO-DNA and CitH3-DNA concentrations in the plasma from mice after sepsis induction by CLP or LPS treated with or without 20 mg/kg As. (**G-I**) Representative images and statistical results of immunofluorescence staining of MPO and CitH3 in lung tissue sections from Sham + Mock, CLP + Mock, Sham + As and CLP + As groups. Scale bars = 50 μm. The data are expressed as means ± SD, $n = 5$ per group. $P < 0.05$ indicate significant differences

the high expression of these cytokines (Fig. 4B-D). The experimental outcomes of dHL60 cells were consistent with those of PBNs (Fig. 4E-G). Furthermore, we measured the NETs biomarkers in the supernatants, including CitH3-DNA complexes and MPO-DNA complexes. The findings showed that under LPS stimulation, the levels of NETs produced by PBNs significantly increased, and treatment with As similarly reduced the high levels of NETs induced by LPS (Fig. 4H-I). The results of dHL60 cells also demonstrated a consistent trend (Fig. 4J-K). Based on the results from both in vitro and in vivo experiments, we could conclude that As could reduce the elevated levels of NETs induced by sepsis.

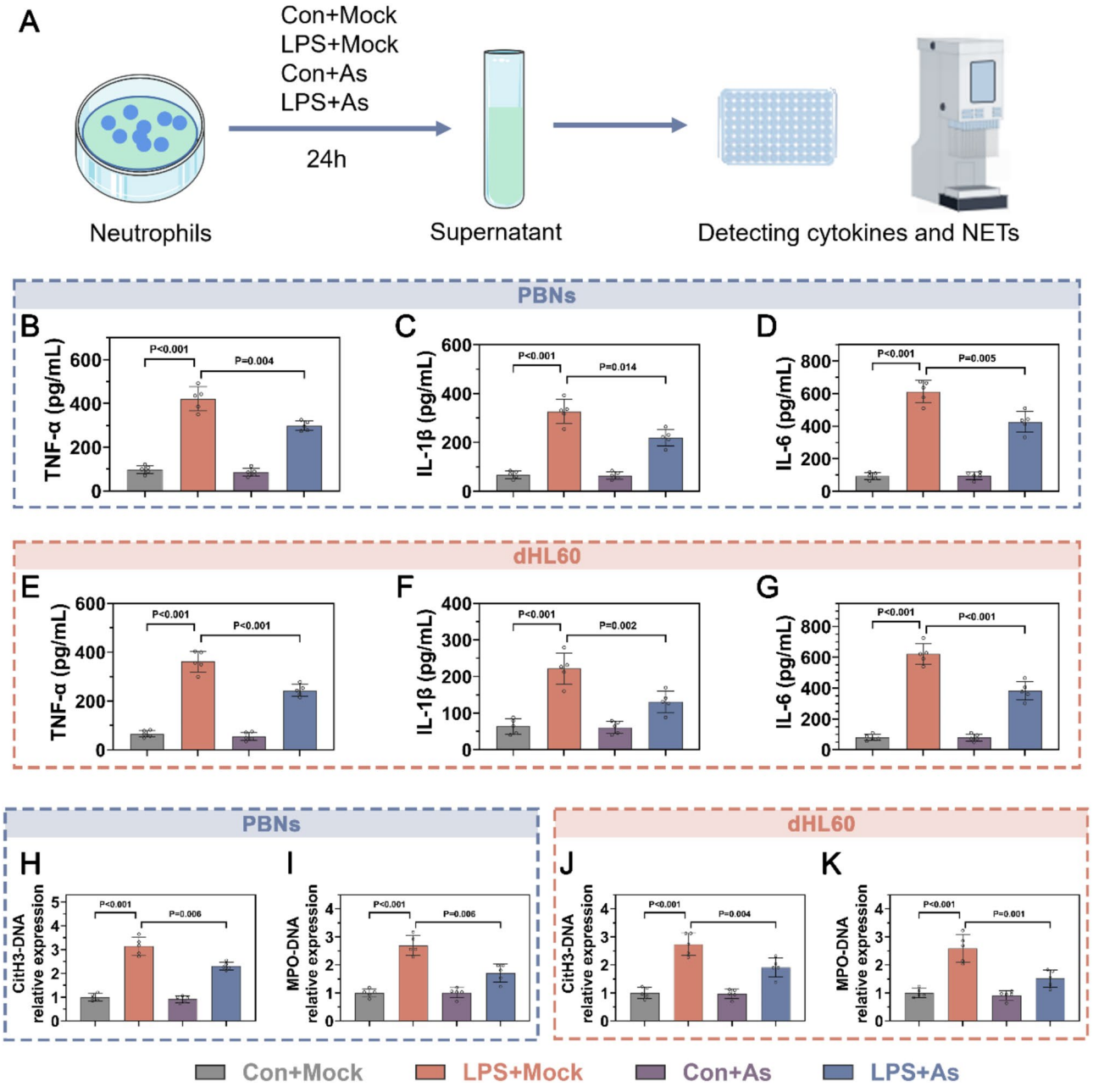

Fig. 4 Astragaloside inhibited NETs and inflammatory response in vitro. (**A**) Diagram of neutrophil culture supernatant collection in which PBNs or dHL60 cells were added with or without LPS or As for 24 h and then collecting cell culture supernatant to detect cytokins or for subsequent experiments. (**B-G**) Concentrations of TNF-α, IL-1β, and IL-6 released into PBNs and dHL60 cell culture supernatants were detected by ELISA in Con + Mock, LPS + Mock, Con + As and LPS + As groups. (**H-K**) Concentrations of CitH3-DNA and MPO-DNA in culture supernatants of PBNs and dHL60 cells with different treatments were determined. The data are expressed as mean ± SD, $n = 5$ per group. $P < 0.05$ indicate significant differences

Astragaloside IV regulated the release of NETs by targeting IκBα to inhibit the NF-κB signaling pathway

Next, we used network pharmacology to search for possible targets of As action on sepsis. We used keyword "Sepsis" to search for sepsis-related genes in OMIM, CTD, GeneCards and GEO databases. Venne diagram showed DEGs that| log2 FC| ≥1.0 and FDR < 0.05 in GSE54514 and genes in OMIM, CTD (scores > 20) and GeneCards (scores > 20) databases (Fig. 5A). We included genes that appeared at least twice. A total of 374 genes were identified as target genes associated with sepsis. Next, the Smile version of As was obtained on Pubchem, and the Smile version was imported into SwissTargetPrediction and SuperPred databases to obtain a total of 266 therapeutic targets of As after removing duplicate targets. Almost 31 target genes of As in the treatment of sepsis

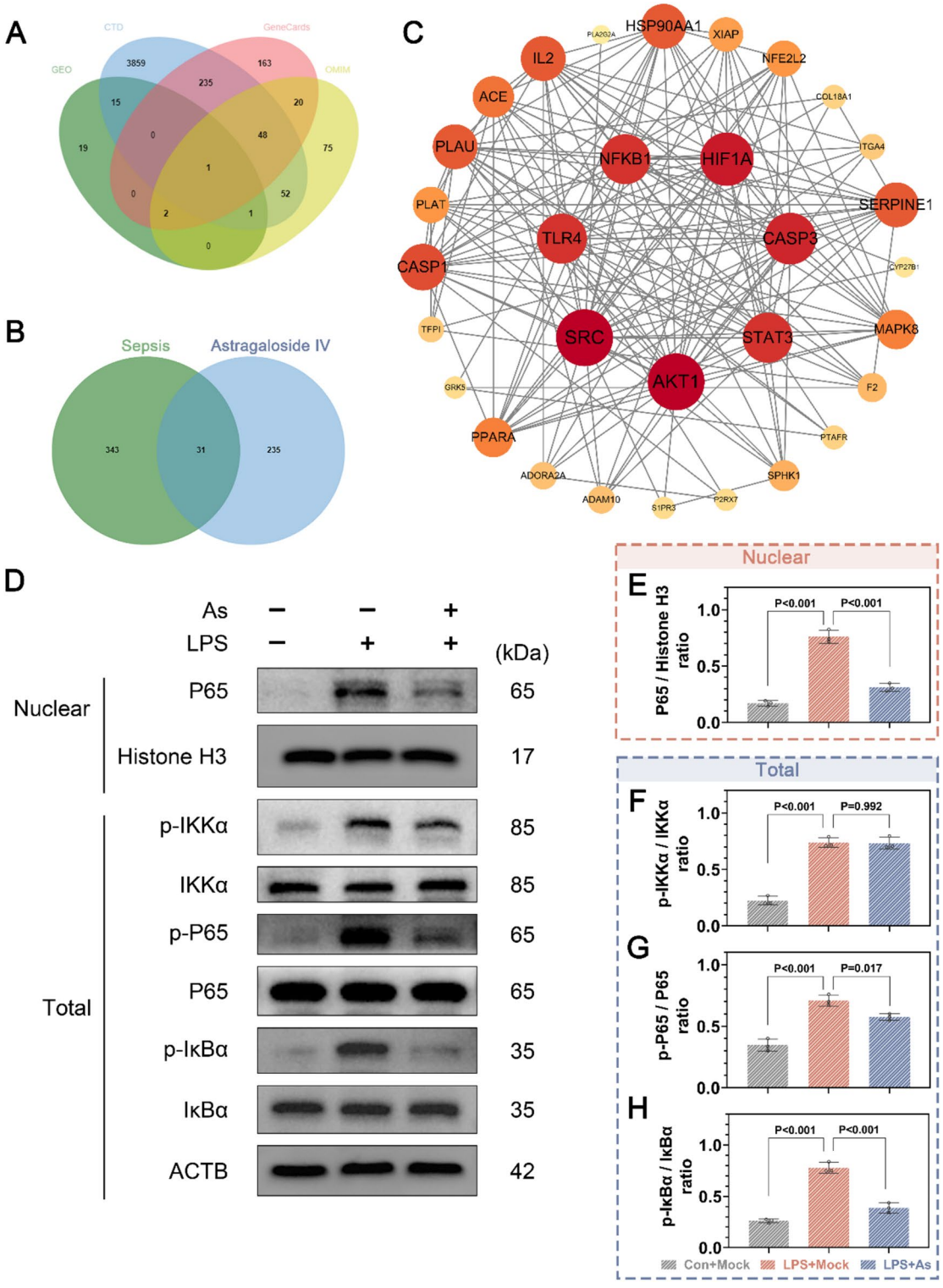

Fig. 5 Astragaloside regulated NETs through NF-κB signaling. (**A**) Venn diagram analysis of sepsis-related genes predicted by the GeneCards, CTD, OMIM and GEO databases. (**B**) Venn diagram analysis of sepsis-related genes and targets of Astragaloside predicted by SuperPred and SwissTargetPrediction databases. (**C**) PPI network analysis of target genes of Astragaloside and sepsis by Cytoscape. The color changes gradually from yellow to red; the closer to the red target gene, the more important it is. (**D-H**) Representative protein bands and statistical values for Nuclear P65 and total p-p65, p65, IKKα, p-IKKα, IκBα and p-IκBα. The data are expressed as mean ± SD, $n = 3$ per group. $P < 0.05$ indicate significant differences

were obtained by intersection of the two (Fig. 5B). The 31 target genes were input into the string database, and Cytoscape software was used to construct the PPI network. A total of 7 Hub targets were obtained, including TLR4, NFκB1, SRC, AKT1, HIF1A, CASP3 and STAT3 (Fig. 5C).

TLR4, sensing of LPS, the most potent pathogen-associated molecular pattern of gram-negative bacteria, activates NF-κB and Irf3, which induces inflammatory cytokines and interferons that trigger an intense inflammatory response, which is critical for the pathogenesis of sepsis [18]. Given the importance of NF-κB signaling in the pathogenesis of sepsis, we examined the expression of NF-κB pathway related proteins in neutrophils. Western blotting analysis revealed that LPS treatment significantly increased the phosphorylation levels of IKKα, IκBα, and P65 in total proteins, and also elevated the level of P65 in nuclear proteins. However, treatment with As reduced the levels of p-IκBα and p-P65 in total proteins, as well as the level of P65 in nuclear proteins. Interestingly, there appeared no significant effect on the p-IKKα levels (Fig. 5D-H). Therefore, As could inhibit the NF-κB signaling pathway in neutrophils during sepsis. Given that As treatment did not affect the level of p-IKKα, but significantly influenced the p-IκBα and the translocation of P65 into the nucleus, we hypothesized that As might regulate the NF-κB signaling pathway by targeting the IκBα.

Docking simulation technology is a convenient and effective method for studying the interactions between small molecules and their target sites. In this study, we employed the Vina 1.1.2 software to conduct a molecular docking study of the binding between As and the IκBα. Our analysis yielded a binding mode diagram of As with the IκBα, where the small molecule As was nestled within a central groove of the protein (Fig. 6A). As formed hydrogen bonds with amino acid residues GLU-153, ASN-145, ARG-143, and ASN-182 on the protein. Additionally, As engaged in hydrophobic interactions with residues ILE-192, LEU-227, LEU-223, and HIS-184 on the protein (Fig. 6B-C). The docking score is an important indicator of the binding energy between a small molecule and a protein, with a score below – 5 kcal/mol typically suggesting a strong binding affinity. In this study, the docking score for the As-IκBα protein complex was – 6.264 kcal/mol (Table S3), indicating that the binding mode was plausible and that As had potential biological activity against IκBα.

To explore the interaction between As and IκBα, we synthesized biotin-labelled As probe (biotin-As) for pull-down analysis. The results showed that IκBα was significantly pulled down by As-beads, and this process could be blocked by an excess of As (Fig. 6D-E). Furthermore, we found that in Drug Affinity Responsive Target Stability (DARTS) analysis, As specifically targeted IκBα to inhibit the proteolytic activity of trypsin (Fig. 6F). Similarly, in CETSA, As significantly prevented the degradation of IκBα protein, but had no effect on the ACTB protein (Fig. 6G-I).

In order to verify the mechanism by which As regulated the level of NETs by inhibiting the NF-κB signaling pathway, we conducted a series of rescue experiments. We transfected P65 overexpression plasmids into PBNs cells and confirmed successful overexpression of P65 through Western blotting analysis (Fig. 6J and Figure S4). As shown in Fig. 6K-L, As treatment could reduce LPS-induced high levels of NETs, including CitH3-DNA complexes and MPO-DNA complexes, while overexpression of P65 could block this reduction effect of As. Meanwhile, we found that As treatment also reduced high levels of LPS-induced TNF-α and IL-1β, while overexpression of P65 could counteract this anti-inflammatory effect of As (Fig. 6M-N). Therefore, As indeed could regulate the release of NETs by inhibiting NF-κB signaling pathway. The above results showed that As targeted IκBα to suppress the activation of NF-κB signaling, thereby regulating the levels of NETs in sepsis.

Neutrophils treated with Astragaloside IV down-regulated tissue cells oxidative stress and death

Organ injury often involves the co-involvement of epithelial cells, endothelial cells and immune cells. It had been proven that elevated NETs often exert toxic effects on other cells. Next, we collected the supernatant of PBNs cell culture after 24 h of treatment from each group and used it for conditioned culture of MLE12 cells (Fig. 7A). Concurrently, the supernatant from dHL60 cell was collected for conditioned culture of HUVEC. Observation of MLE12 cell death using a live/dead cell staining assay clearly showed a significant increase in the number of dead cells in the LPS + Mock group, while the number of dead cells decreased after treatment with As (LPS + As group) (Fig. 7B). Furthermore, the CCK-8 assay results indicated that cell proliferation was markedly inhibited in the LPS + Mock group, and there was a recovery in cell proliferation capacity after treatment with As (LPS + As group) (Fig. 7C-D).

To investigate whether As mitigated tissue cell damage in sepsis by regulating NETs, we conducted a series of rescue experiments. Initially, PAD4 overexpression plasmids were transfected into PBNs cells, and the successful overexpression of PAD4 was confirmed using Western blotting technology (Figure S5A-B). As shown in Figure S5C-F, overexpression of PAD4 attenuated the inhibitory effect of AS on CitH3-DNA, MPO-DNA, TNF-α, and IL-1β. Additionally, we collected the supernatant from PBNs and dHL60 cells in the LPS + Mock + OE-NC group, LPS + As + OE-NC group, and LPS + As + OE-PAD4 group to treat MLE12 and HUVEC cells. CCK-8

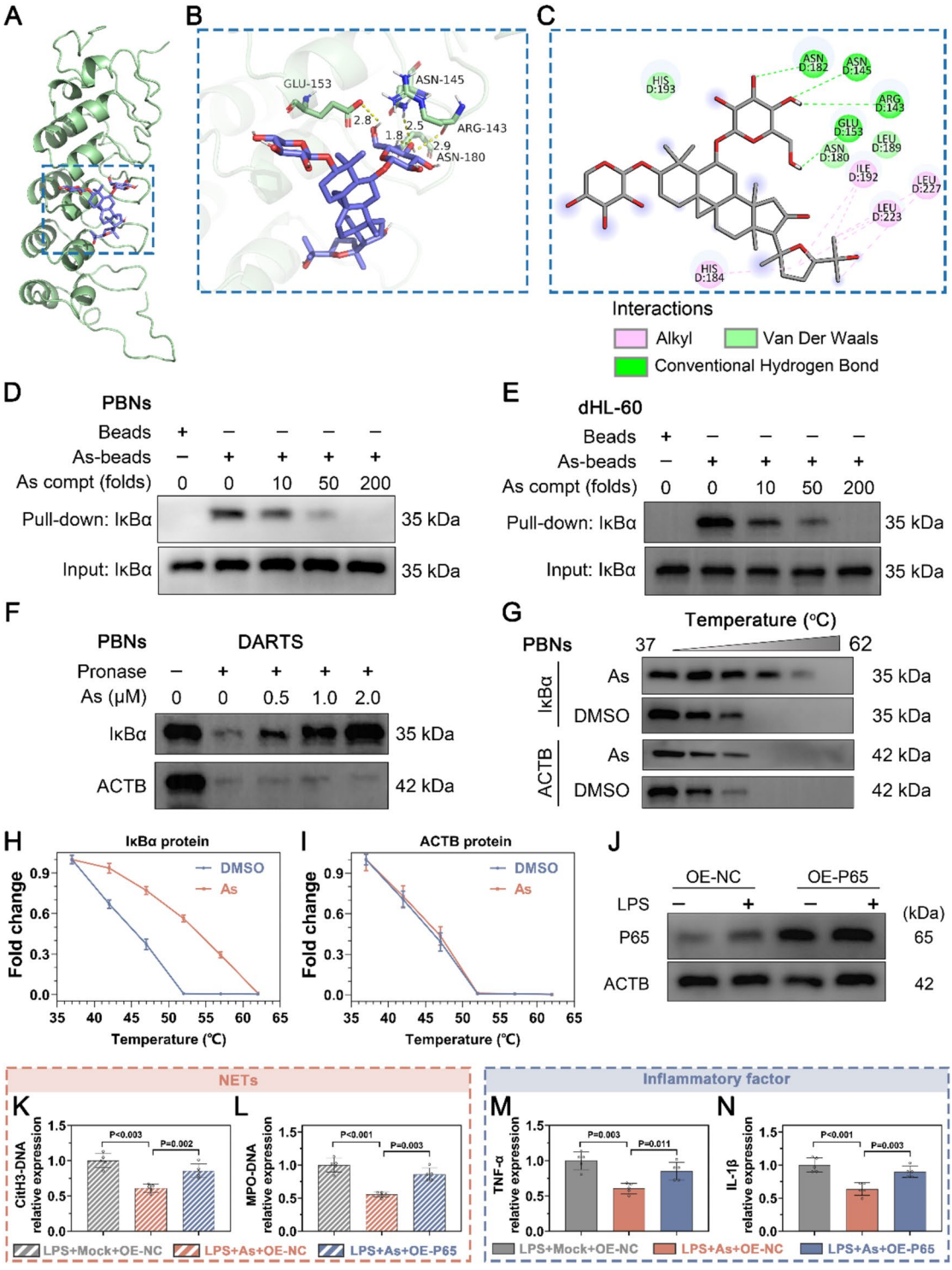

Fig. 6 Astragaloside IV could bind to IκBα. (**A-B**) Representative images of the docking mode of As binding to IκBα. (**C**) The potential connection sites between As and IκBα. (**D-E**) PBNs cells and their lysates were incubated with As-biotin, followed by pull-down assay using streptavidin beads. The results showed immunoblot analysis of the IκBα protein. (**F**) After incubation with As, the lysates of PBNs cells were treated with proteinase K. The results demonstrated immunoblot analysis of both IκBα and ACTB proteins. (**G**) CETSA assay to confirm binding of As to IκBα. (**H-I**) presented representative blot and protein results. (**J**) Representative blots of P65 overexpression in PBN cells. (**K-N**) PBN cells were transfected with P65 overexpression or NC plasmid for 24 h and added with or without As along with LPS to continuous cultivation for 24 h, then the concentration of NETs and inflammatory factors in the supernatant were detected. (**K-L**) Concentrations of CitH3-DNA and MPO-DNA from three groups. (**M-N**) Concentrations of TNF-α and IL-1β from three groups. The data are expressed as mean ± SD, ($n = 3$ for D-J, $n = 5$ for K-N). $P < 0.05$ indicate significant differences

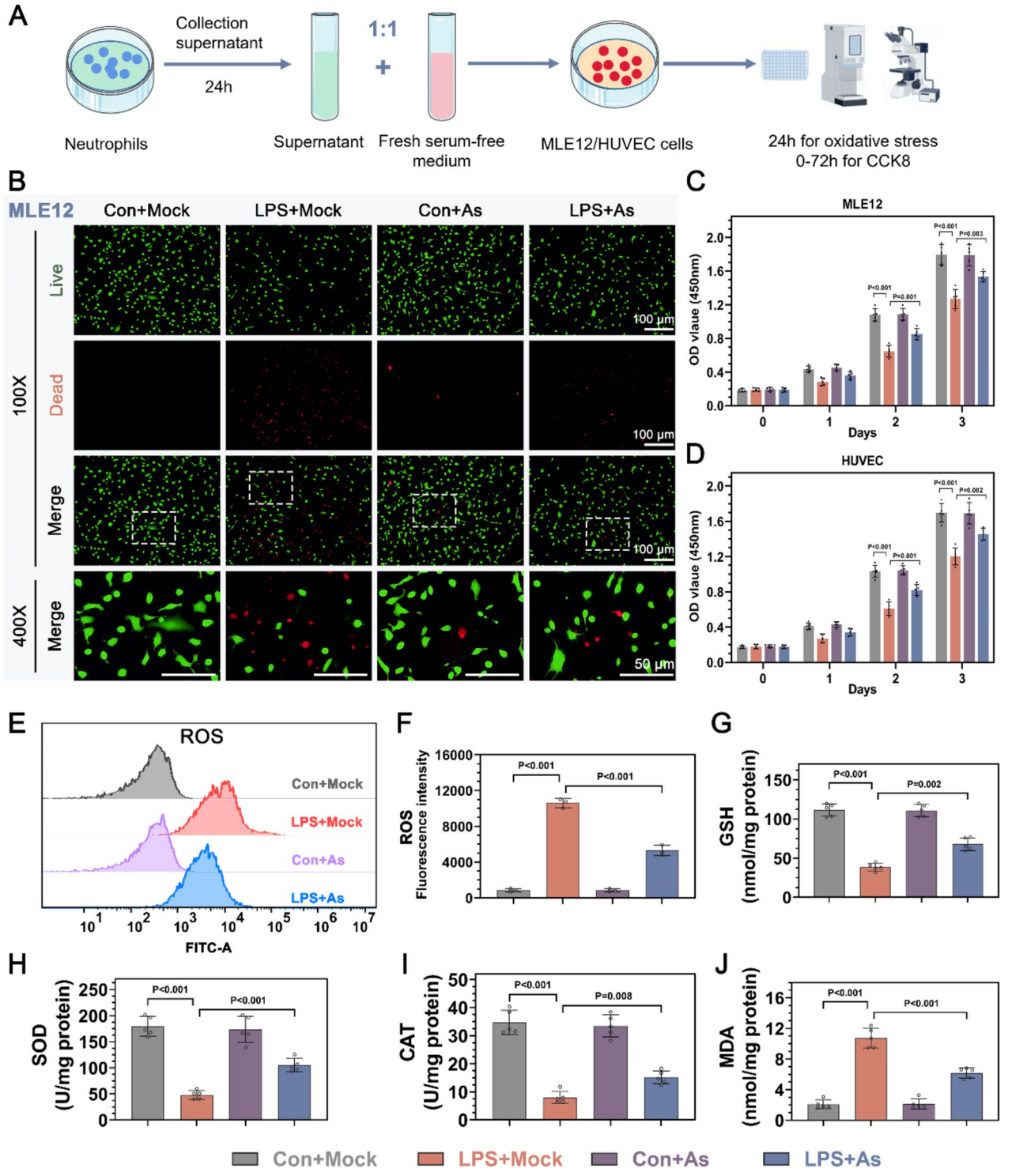

Fig. 7 As treated neutrophils inhibited apoptosis and oxidative stress of lung epithelial cells. (**A**) Schematic representation of neutrophil supernatant treating tissue cells. Neutrophils with different treatments were cultured for 24 h and then replaced with fresh medium. After continued culture for 24 h, supernatant was collected by centrifuge and then used as conditioned medium (CM). HUVEC or MLE12 cells were added into CM and fresh medium of 1:1 for culture for 24 h to detect oxidative stress and apoptosis, and to detect cell proliferation for 24–72 h. (**B**) Representative staining of live and dead cell staining of MLE12 cells. The box shows a 400X magnification of the location. Scale bars = 100 μm–50 μm. (**C-D**) CCK-8 assay to detect cell proliferation of HUVEC and MLE12 cells in different groups. (**E**) DCFH-DA-stained MLE12 cells were tested via flow cytometry, which also represented the ROS content in the cells. In the representative images of flow, the vertical coordinate represented the number of cells and the horizontal coordinate represented the fluorescence intensity of DCFH-DA. (**F**) Quantitative values of DCFH-DA fluorescence intensity. (**G-J**) The levels of GSH, SOD, CAT and MDA in MLE12 cells, which represented oxidative stress, were measured. The data are expressed as mean ± SD, $n = 5$ per group. $P < 0.05$ indicate significant differences

assay results showed that the cell proliferation rate of the LPS + As + OE-NC group was higher than that of the LPS + Mock + OE-NC group, while the cell proliferation rate of the LPS + As + OE-PAD4 group was lower than that of the LPS + As + OE-NC group (Figure S5G-H). In view of the regulatory effect of NF-κB on NETs, we further treated HUVEC and MLE-12 cells with neutrophil CM overexpressing P65. The CCK-8 experiment further proved our conclusion, in which the cell proliferation rate of the LPS + As + OE-P65 group was significantly lower than that of the LPS + As + OE-NC group (Figure S6A-B).

To further explore the underlying mechanisms of neutrophils damage tissue cells, we continued to treat MLE-12 cells with CM. Figure 7E-F showed significantly increase of ROS levels in LPS + Mock MLE12 cells, which was reduced in LPS + As group. Subsequently, to assess the damage to the cells' antioxidant capacity, glutathione (GSH), superoxide dismutase (SOD), and catalase (CAT) were measured in MLE12 cells after conditional culture treated in each group. The results indicated that the conditional culture of the LPS + Mock group led to a decrease in GSH levels and a reduction in SOD and CAT enzyme activities within MLE12 cells, while the conditional culture following As treatment (LPS + As group) partially restored these indicators (Fig. 7G-I). Finally, we analyzed the level of lipid peroxidation within the cells by measuring the content of malondialdehyde (MDA). The results showed that the conditional culture of the LPS + Mock group significantly increased the level of MDA within MLE12 cells, while the conditional culture following As treatment (LPS + As group) reduced these levels (Fig. 7J). In summary, As, modulating the levels of NETs, alleviated the oxidative stress-induced damage and death.

Preparation and characterization of ZIF-8, As@Z, and As@ZM

In order to improve the stability and bioavailability of As, it was urgent to develop new materials based on As. Metal-organic frameworks (MOFs) are materials composed of metal ions, clusters, or organic linkers. In the field of drug delivery, MOFs, as emerging carriers, have demonstrated their high drug-loading capacity, ease of surface modification, and the ability to achieve controlled drug release. Zeolitic imidazolate framework-8 (ZIF-8), a member of the zeolitic imidazolate frameworks (ZIFs), is primarily composed of zinc ions and 2-methylimidazole (2-MIM). In this study, we utilized ZIF-8 as a carrier for the delivery of astragaloside IV (As), and coated the outermost layer with a neutrophil membrane. Using this method, we prepared three types of nanoparticles: ZIF-8, As-loaded ZIF-8 (As@ZIF-8, abbreviated as As@Z), and neutrophil membrane-coated As@Z (As@ZIF-8/Neutrocyte membrane, abbreviated as As@ZM). The preparation process of these nanoparticles was depicted in Fig. 8A. The structural formula of As was displayed in Figure S1. During the synthesis of As@ZM, we observed through the encapsulation efficiency (LE) and encapsulation rate (EE) test results that the dosage of 20 mg/mL of As achieved the optimal levels of LE and EE, thus being selected as the preferred dosage for subsequent synthesis (Figure S7). The morphology of ZIF-8 and As@ZM was observed using SEM (Fig. 8B). The results showed that ZIF-8 exhibited a hexagonal structure with sharp edges, while As@ZM nanoparticles appeared more rounded, tending towards a spherical or elliptical shape. Further observation using TEM (Fig. 8C) revealed that As@ZM had a typical core-shell structure with an average coating thickness of approximately 20 nm. We further measured the zeta potential and hydrated particle size of ZIF-8, As@Z, and As@ZM nanoparticles. The results showed that the zeta potential of ZIF-8 was 22.02 mV, while that of As@ZM was −18.48 mV (Fig. 8D). The decrease in potential could be attributed to the negatively charged nature of the cell membrane, and this lower negative potential was beneficial for the nanoparticles to maintain suspension, dispersion, and stability in the bloodstream. The hydrated particle size increased from 201.56 nm for ZIF-8 to 227.62 nm for As@ZM (Fig. 8E), with this increase in particle size mainly due to the coating of the outer cell membrane. The presence of cell membrane proteins in As@ZM was further confirmed by SDS-PAGE. The results indicated that As@ZM displayed a protein spectrum identical to that of the neutrophil membrane, suggesting that As@ZM nanoparticles were successfully encapsulated by the neutrophil membrane (Fig. 8F). Thermogravimetric analysis (TGA) showed a gradual increase in the organic component content of ZIF-8, As@Z, and As@ZM (Fig. 8G). Additionally, we monitored the changes in hydrated particle size of the nanoparticles in PBS over a 7-day period. The results showed that the particle sizes of ZIF-8, As@Z, and As@ZM nanoparticles only slightly decreased over the 7-day observation period (Fig. 8H), indicating that the prepared nanoparticles had high physicochemical stability in PBS solution. X-ray photoelectron spectroscopy (XPS) analysis further confirmed the presence of carbon (C), nitrogen (N), phosphorus (P), sulfur (S), oxygen (O), and zinc (Zn) in As@ZM (Fig. 8I). Based on these experimental results, we could conclude that ZIF-8, As@Z, and As@ZM nanoparticles were successfully prepared, and they all exhibited good physicochemical stability.

As@ZM exhibited good biocompatibility, the ability to specifically target neutrophils, and controlled release characteristics of As

Good biocompatibility is always considered a fundamental requirement for the biomedical applications of nanomaterials. To evaluate the biocompatibility of the

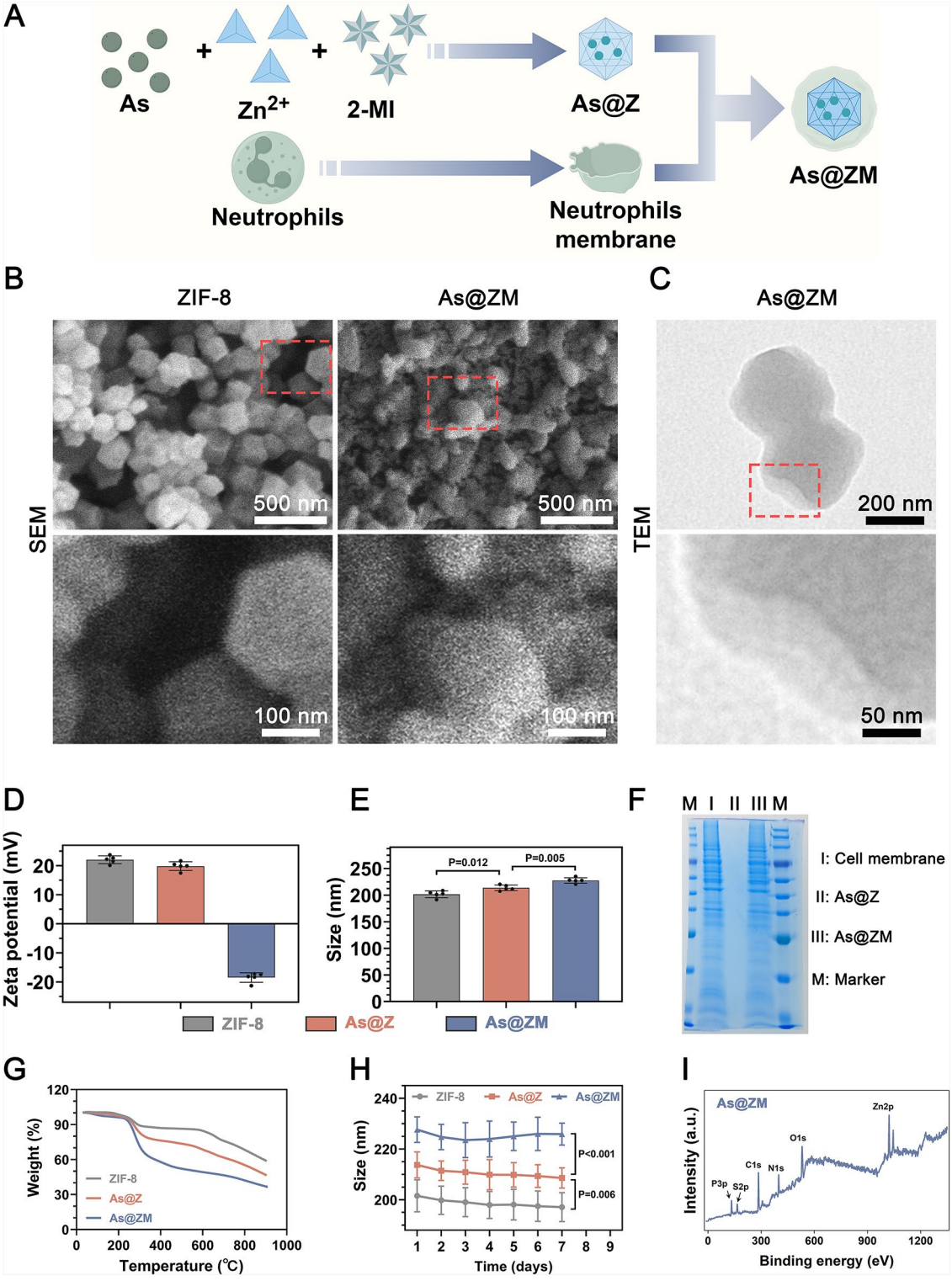

Fig. 8 Preparation and characterization of ZIF-8, As@Z, and As@ZM. (**A**) Schematic representation of the synthesis of As@ZM. (**B**) SEM images of ZIF-8 and As@ZM (low magnification scale bar: 500 nm, high magnification scale bar: 100 nm). (**C**) TEM images of As@ZM (low magnification scale bar: 200 nm, high magnification scale bar: 50 nm). (**D**) Zeta potentials of the different nanoparticles and (**E**) hydrated particle sizes. (**F**) SDS-PAGE protein analysis of the Neutrophil membrane, As@Z, and As@ZM. (**G**) Thermogravimetric analysis (TGA) curves of ZIF-8, As@Z, and As@ZM. (**H**) Changes in hydrated particle size of ZIF-8, As@Z, and As@ZM over 7 days. (**I**) XPS spectrum of R@ZQC. All the data in D, E, and H are presented as the mean ± SD, $n = 5$ per group. $P < 0.05$ indicate significant differences

biomimetic nanoparticles (As@ZM) we prepared, we co-cultured As@ZM nanoparticles at various concentration gradients (10, 20, 30, 40 μg/mL) with diluted mouse blood to assess whether As@ZM would cause hemolysis. The experimental results showed that at a concentration of 20 μg/mL, the hemolysis rate caused by As@ZM nanoparticles was 2.47% (± 1.38%), which was not significantly different from the hemolysis rate of the negative control group. This indicated that As@ZM nanoparticles at concentrations of 20 μg/mL and below essentially did not cause hemolysis and exhibited good biocompatibility (Fig. 9A-B). Additionally, we administered As@ZM nanoparticles at varying concentration gradients (10, 20, 30, 40 mg/kg) via tail vein injection into mice and collected the main organs (heart, liver, and kidneys) for H&E staining after two weeks. The results showed no pathological changes in these major organs at all tested concentrations, further confirming the excellent in vivo safety profile of As@ZM nanoparticles (Fig. 9C).

After confirming the successful synthesis of As@ZM nanoparticles with stable physicochemical properties and good biocompatibility, we further explored the potential advantages of As@ZM nanoparticle treatment over the sole use of As treatment. We first investigated the targeting of As@ZM nanoparticles to neutrophils. The results demonstrate that, compared to the PBS control group, both RAW 264.7 and PBNs cells exhibit increased fluorescence intensity after incubation with As@Z and As@ZM (Fig. 9D). Notably, for RAW 264.7 cells, the fluorescence intensity is similar between the As@Z and As@ZM treatment groups. However, PBNs cells treated with As@ZM show significantly higher fluorescence intensity compared to those treated with As@Z (Fig. 9D), confirming the specific targeting of neutrophils by As@ZM in vitro.

Furthermore, we have performed immunofluorescence staining of lung tissues to verify the targeting ability of As@ZM to neutrophils in vivo. The red fluorescence signals (representing neutrophils stained with Ly6G) in the lung tissues of all sham-operated mice are almost identical. Similarly, the red fluorescence signals in the lung tissues of all mice undergoing CLP surgery are comparable. Importantly, the red fluorescence is markedly increased in the CLP group compared to the sham group, indicating enhanced neutrophil infiltration in the lung tissues of CLP mice. Crucially, the green fluorescence intensity in the CLP + As@ZM group is significantly higher than that in the CLP + As@Z group (Fig. 9E). Further analysis reveals minimal colocalization between neutrophils and As@Z nanoparticles, whereas a high degree of colocalization is observed between neutrophils and As@ZM (Fig. 9F and S8). These findings further substantiate the targeting ability of As@ZM to neutrophils in vivo.

Additionally, we analyzed the release characteristics of As from As@Z and As@ZM nanoparticles. The release of As was effectively controlled through the encapsulation by the ZIF-8 carrier and the neutrophil membrane (Fig. 9G). This helped to reduce the fluctuations in the blood concentration of As in mice, maintaining the blood concentration within an effective and low side effect range for a longer period, thereby improving the therapeutic effect while reducing side effects. We further investigated the specific effects of nanoparticles on the stability and bioavailability of As. The stability of As in the nanoparticles was assessed by measuring the retention rate after long-term storage (30 days at 25 °C under natural light), high-temperature treatment (50–90 °C), and UV light exposure. The results indicated that the stability of As was improved in both As@Z and As@ZM nanoparticles, with As@ZM showing even more significant enhancement (Figure S9 A-C). Additionally, we evaluated the bioavailability of As in mice after intravenous injection of As, As@Z, and As@ZM nanoparticles. The results showed that the $AUC_{0\text{-}t}$ for As was 12.19 ± 1.01 (μg/mL)·h, while the $AUC_{0\text{-}t}$ for As@Z and As@ZM were 14.94 ± 0.58 and 18.02 ± 0.88 (μg/mL)·h, respectively (Figure S9D, Table S4). This indicates that the bioavailability of As@Z and As@ZM was 1.26 and 1.48 times that of As alone.

Based on the above experimental results, we could conclude that we had successfully synthesized As@ZM nanoparticles, which exhibited stable physicochemical properties and good biocompatibility. Compared with the treatment using As alone, As@ZM nanoparticles demonstrate multiple advantages such as targeting neutrophils, regulating the release of As, significantly enhancing the stability of As, and effectively improving the bioavailability of As. These characteristics endow them with potential broad prospects for clinical application.

The therapeutic efficacy of As@ZM nanoparticles in the treatment of sepsis was superior to that of monotherapy with As

After an in-depth investigation of the biocompatibility and unique advantages of As@ZM nanoparticles, we further explored their therapeutic effects on a sepsis mouse model. CLP mouse were administered with drug or nanoparticles via tail vein injection once daily for 3 days prior to the surgery at a dosage of 20 mg/kg. Peripheral blood was collected from the mice 12 h post-surgery, and lung, liver, and kidney tissues were harvested 24 h post-surgery. Mouse survival was continuously monitored and recorded, and a 7-day survival curve was plotted (Fig. 10A). Initially, we analyzed and plotted the 7-day survival curve of the mice. The results showed that the 7-day survival rate of the mice in the CLP surgery group treated with As alone was 50.0% (10/20), while the survival rate in the As@ZM treatment group reached 65.0% (13/20), demonstrating that As@ZM was more effective

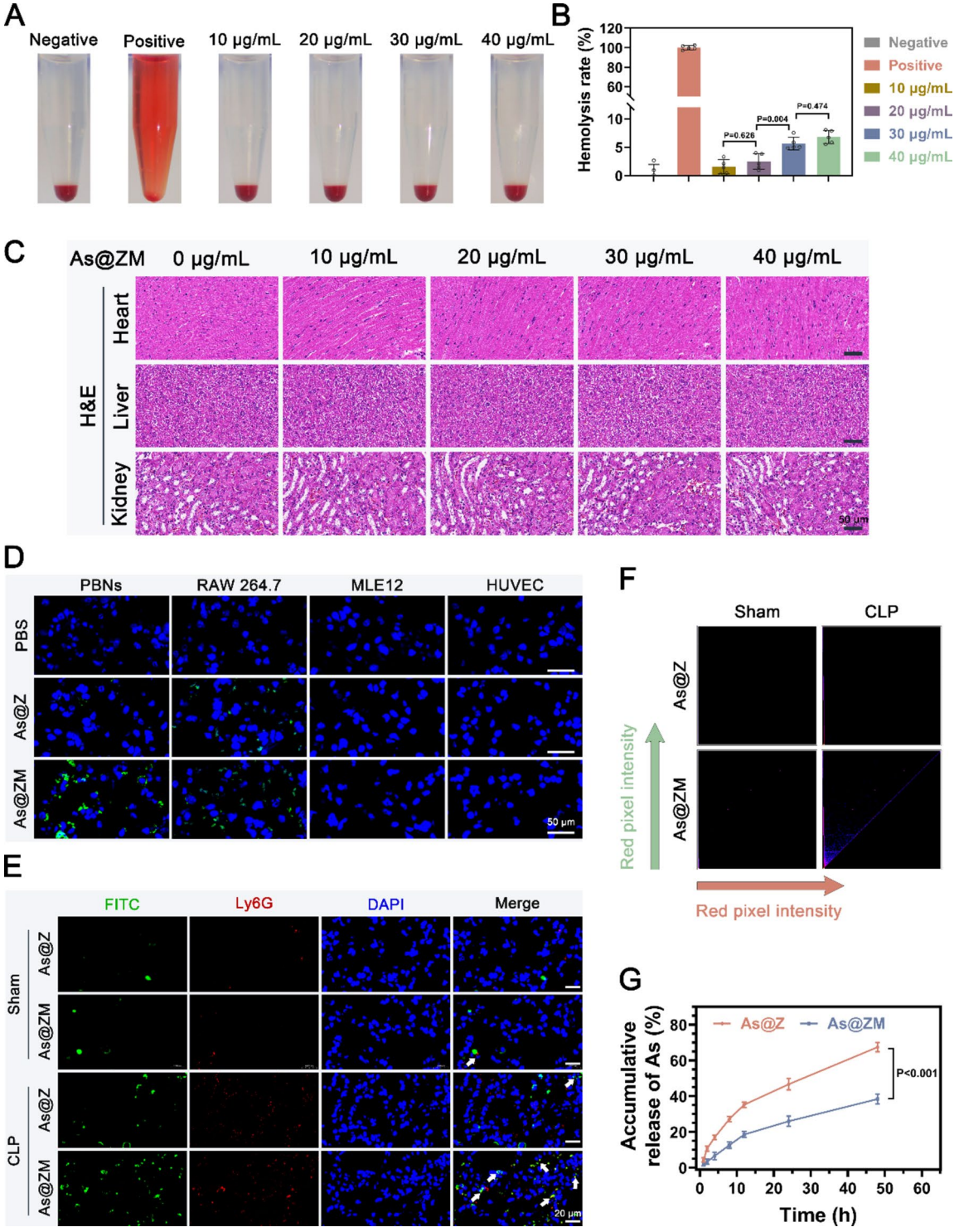

Fig. 9 As@ZM exhibited good biocompatibility, the ability to specifically target neutrophils, and controlled release characteristics of As. (**A-B**) Representative photographs of diluted blood samples after various treatments, along with quantitative analysis of the hemolysis rate. (**C**) H&E staining images of major organs such as the heart, liver, and kidney two weeks post different treatments (Scale bar: 100 μm). (**D**) Confocal Laser Scanning Microscopy (CLSM) images of various cell lines incubated with FITC-labeled As@Z nanoparticles or As@ZM nanoparticles for 4 h (Scale bar: 50 μm). (**E**) Three hours after the mice underwent sham surgery or CLP surgery, they were injected with anti-Ly6G antibody (red) and FITC-labeled nanoparticles (green) via the tail vein. Thirty minutes later, the lung tissues of the mice were collected for fluorescence detection. (**F**) Representative two-dimensional intensity histogram from Figur 9E. The y-axis represents the intensity of green pixels above zero (FITC-labeled nanoparticles). The x-axis represents the intensity of red pixels above zero (neutrophils). (**G**) In vitro release profile of As from As@Z and As@ZM treated with PBS within 48 h. All the data in B, and E are presented as the mean ± SD, $n = 5$ per group. $P < 0.05$ indicate significant differences

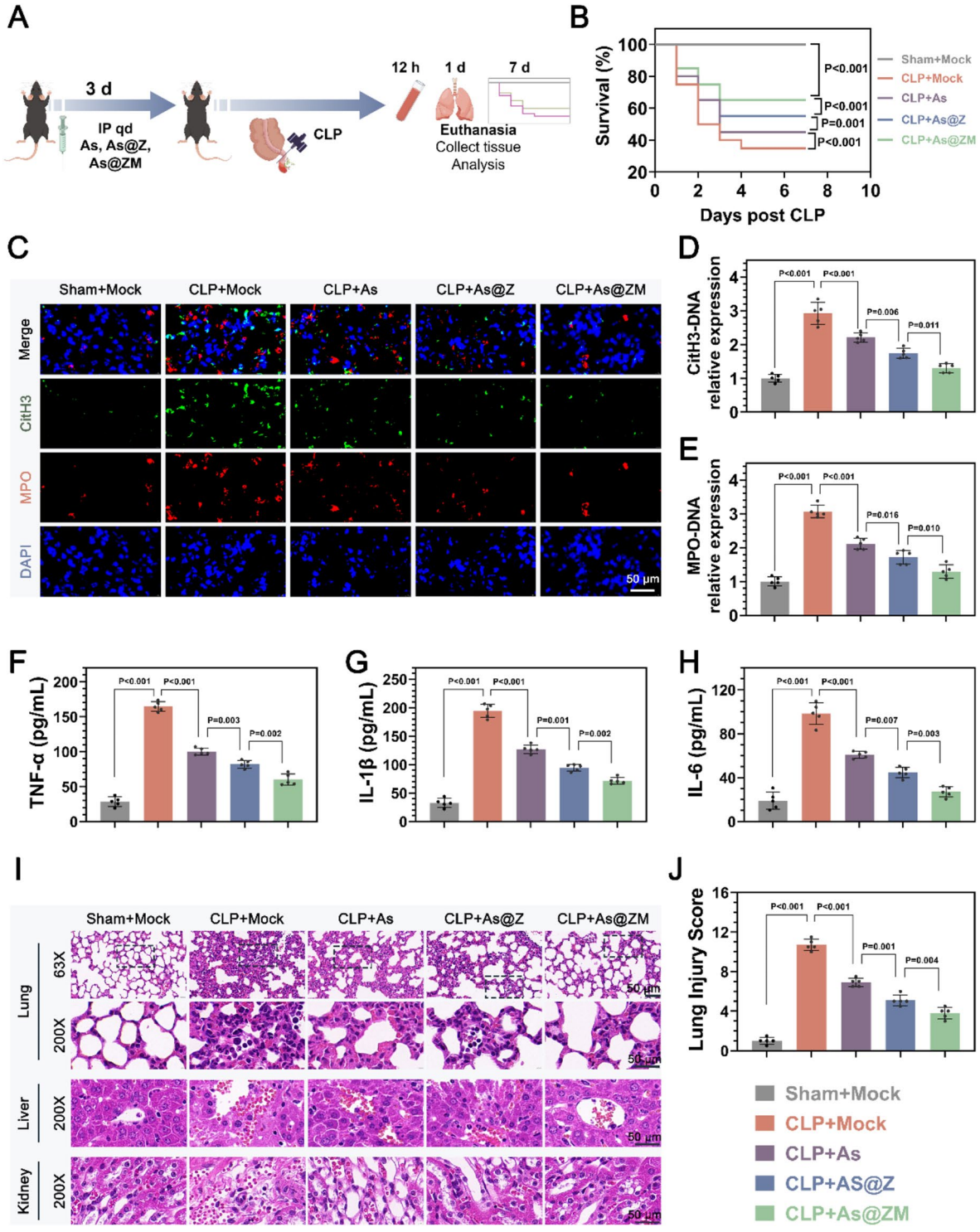

Fig. 10 The therapeutic efficacy of As@ZM nanoparticles in the treatment of sepsis was superior to that of monotherapy with As. (**A**) Schematic diagrams of animal model establishment, sample collection, and treatment processes with As, As@Z, and As@ZM. (**B**) Survival curves of mice over 7 days ($n = 20$). (**C**) Immunofluorescence technique was used to detect key components of NETs, including MPO and CitH3, in mouse lung tissue. (**D-E**) ELISA was employed to measure the levels of NETs biomarkers in mouse peripheral blood, specifically CitH3-DNA complexes and MPO-DNA complexes. (**F-H**) ELISA was also used to detect the levels of inflammatory cytokines in mouse peripheral blood, including TNF-α, IL-1β, and IL-6. (**I**) Assessment of organ damage in major organs (lung, liver, kidney) of mice by H&E staining. (**J**) Lung tissue damage scores derived from the analysis of H&E stained images of mouse lung tissue. All the data in D, E, F, H, I, and J are presented as the mean ± SD, ($n = 20$ for B, $n = 5$ for C-J). $P < 0.05$ indicate significant differences

in improving the 7-day survival rate of CLP-induced septic mice than As monotherapy (Fig. 10B). Meanwhile, IF and ELISA results indicated that As@ZM was more effective in inhibiting NETs levels and cytokines in CLP-induced septic mice than As monotherapy (Fig. 10C-H). The extent of organ damage in CLP-induced septic mice (lung, liver, kidney) was assessed using H&E staining, lung injury scoring, protein content in BALF, ALT, AST, creatinine, BUN, and other indicators. The results further confirmed that As@ZM was more effective in reducing organ damage compared to As monotherapy (Fig. 10I-J, Figure S10A-E). Additionally, we conducted in vitro experiments to assess the therapeutic potential of As@ZM nanoparticles against cell damage induced by NETs. CCK-8 assay results indicated that As@ZM nanoparticles were more effective in restoring the proliferative vitality of MLE12 cells than the treatment with As alone (Figure S11). Considering the aforementioned experimental outcomes, we could conclude that, due to the excellent biocompatibility and unique therapeutic advantages of As@ZM nanoparticles, their efficacy in treating sepsis was significantly enhanced compared to the use of As alone.

Discussion

Although NETs play an important role in trapping infections such as bacteria, excess NETs have been associated with excessive inflammatory responses, autoimmune enhancement, and vascular thrombosis, becoming potentially harmful mediators of immune-related organ failure [4, 19]. When sepsis occurs, the normal apoptosis of neutrophils is inhibited, the lifespan of neutrophils is prolonged, and the neutrophils transition to inflammatory NETosis [20]. Our study also observed abnormal increases in MPO-DNA and CitH3-DNA, the core components of NETs in peripheral blood of patients with sepsis, which were significantly positively correlated with the pro-inflammatory factors IL-1β and TNF-α, and neutrophils were also aggregated in the lung tissue of CLP mice. Given that inflammatory cytokine storms are an important feature of sepsis, reducing the release of NETs is a promising therapy for the treatment of immune disorders [21, 22]. The use of As in both CLP or LPS-induced sepsis mouse models reduced the release of NETs and improved mouse survival, lung tissue damage and liver and kidney function.

Considering that the core components of NETs are located in the nucleus, we did not research the direct interaction between As and NETs components. Network pharmacologic screening of the NF-κB signaling pathway acts As a mediator between AS and NETs (Fig. 5). The key step in the formation of NETs is the histone citrullination catalyzed by PAD4 [23]. Sun et al. expanded several peptidyl arginine deiminase (pad), including PAD2-4, which can directly citrulline p65, enhance p65 into the nucleus, and thus up-regulate the release and secretion of the NF-κB-dependent cytokines IL-1β and TNF-α [24]. NETs induced by cigarette smoke extract also promoted the activation of NF-κB, and further studies revealed the role of the cGAS/TLR9 signaling pathway in DAMP recognition of NETs-DNA [25]. Conversely, Yu et al. found that celastrol effectively inhibited neutrophil oxidative rupture and NET formation induced by different inflammatory stimuli by down-regulating the SYK-MEK-ERK-NF-κB signaling cascade [26]. This reveals the biphasic interaction of NF-κB with NETs. Our study also demonstrated that inhibition of NF-κB or overexpression of P65 could affect the level of NETs and the secretion of related inflammatory factors.

In the typical NF-κB signaling pathway activated by LPS, the MYD88, TRAF6, and IKK complexes are activated sequentially, ultimately leading to phosphorylation and degradation of IκB [27]. Degradation of IκB releases p65/p50 dimers, which are then carried into the nucleus via imported proteins [28]. Our results demonstrated that As regulated the nuclear shift of P65 by binding to IκBα rather than IKKα. Previous studies by Huang [12] and Zhu [29] demonstrated the inhibitory effect of As on p-IKK, which we did not observe in our study. One possible reason is that As does not play exactly the same role in different cell types, such as neutrophils or cardiomyocytes.

The formation of NETs also affects the function of other cellular components of the body. Components of NETs, such as histones and DNA, are cytotoxic and can damage endothelial cells [4, 30]. It releases tissue factors that promote platelet activation and aggregation. NETs can also induce pyroptosis or M1 polarization of macrophages, exacerbating the inflammatory response during sepsis, which may be attributed to exosomes or inflammatory factors secreted by neutrophils [2, 31]. In our in vitro experiments, LPS-treated neutrophil supernatants significantly inhibited the proliferation of MLE12 and HUVEC cells and induced cell death, accompanied by increased oxidative stress in lung epithelial cells. This is another piece of evidence that NETs damage endothelial cells. Other studies have included promotion of sinusoidal endothelial cell segregation, impairment of vascular reactivity, and activation of MMP-2 leading to endothelial dysfunction [32, 33]. However, we did not further explore the signaling molecules that mediate communication between neutrophils and other cells.

Although As has been effective in the treatment of organ damage caused by inflammation, and our study observed a huge improvement in sepsis with As, there is still a long way to go when translating these results into clinical practice. We must recognize the complexity of sepsis pathophysiology, and the role of macrophages and T cells in sepsis should not be underestimated. Targeting

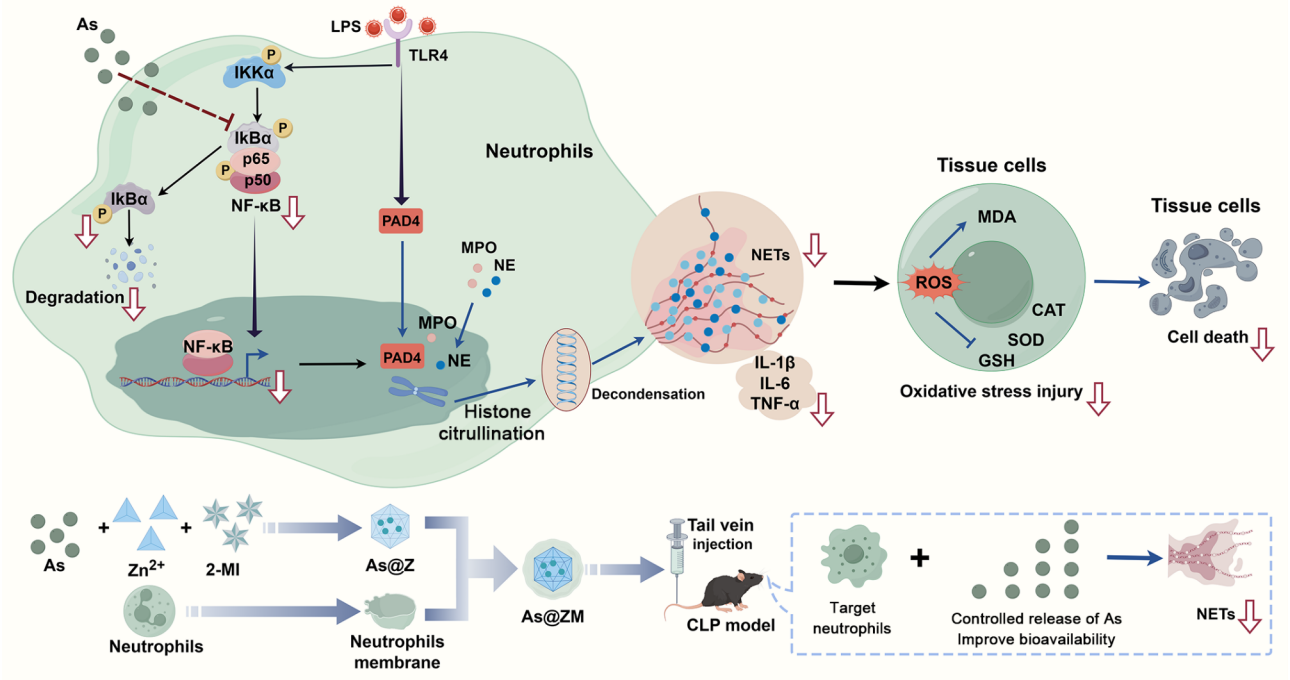

Scheme 1 The diagram outlines the novel mechanism of Astragaloside IV (As) in regulating NETs production through targeted binding to IκBα, as well as the application of Astragaloside IV-loaded biomimetic nanoparticles (As@ZM) in inhibiting neutrophil extracellular traps (NETs) and treating sepsis

NETs alone may not be sufficient to fully address the complex interactions between pathogens, cytokines, and tissue damage. Combination therapy targeting multiple aspects of sepsis, including but not limited to the NETs and NF-κB pathways, is needed to achieve potential synergies in reducing inflammation and improving primary target organ function. In addition, considering the important function of NETs itself in pathogen clearance and microbiome maintenance, blind excessive elimination of NETs is not advisable to avoid minimize disruption of host defense mechanisms.

Although we have demonstrated that As exhibits a certain therapeutic effect on sepsis, the efficacy remains unsatisfactory (only increasing the 7-day survival rate of CLP mice by approximately 10-15%). Therefore, we innovatively designed and prepared a nanodelivery system aimed at achieving targeted delivery and controlled release of As, with the goal of enhancing its therapeutic effect in sepsis treatment. In this study, we selected ZIF-8 nanoparticles as the carrier, loaded them with As internally, and coated them with neutrophil membranes externally, successfully constructing As@ZM nanoparticles. Further research revealed that, compared to the treatment regimen using As alone, As@ZM nanoparticles exhibited significant advantages in targeting neutrophils, regulating As release, markedly enhancing As stability, and effectively improving its bioavailability. These characteristics endow them with broad potential for clinical application. The final results indicated that, compared to As alone, As@ZM nanoparticles demonstrated more pronounced superiority in reducing NETs levels, alleviating inflammatory responses, improving organ damage, and enhancing the 7-day survival rate of septic mice.

In conclusion, this study found another new mechanism of As in the treatment of sepsis, that is, As could indirectly inhibit the release and activation of P65 by binding with IκBα, and reduce the release of NETs to inhibit inflammatory factors. At the same time, neutrophil conditioned medium treated with As could inhibit oxidative stress and death of endothelial cells and lung epithelial cells, which together reduced the damage of important target organs such as lung, liver and kidney in sepsis. Finally, we characterized a new nanomaterial, which could significantly improve the efficacy of As and was promising to treat sepsis clinically in the future (See Scheme 1).

Abbreviations

As	Astragaloside IV
CCK-8	Cell counting kit-8
CETSA	Cellular thermal shift assay
CLP	Cecum ligation and puncture
CM	Conditioned medium
DAMP	Damage-associated molecular patterns
ELISA	Enzyme-linked immunosorbent assay
LPS	Lipopolysaccharide
NETs	Neutrophil extracellular traps
NF-κB	Nuclear transcription factor-κB
PBS	Phosphate-buffered saline
TEM	Transmission electron microscopy

Supplementary Information

The online version contains supplementary material available at https://doi.org/10.1186/s12951-025-03260-x.

Supplementary Material 1

Author contributions

S. W. Designed experiments and wrote manuscript. M. Z. Collected the specimens and developed the experiments. H. Z. Analyze the data. L. H. Helped to perform the experiments. H. L. Supervision, Funding acquisition. All the authors have read and approved the final version of the manuscript.

Funding

This study was supported by the Program of Excellent Doctoral (Postdoctoral) of Zhongnan Hospital of Wuhan University (Grant No. ZNYB2023003).

Data availability

No datasets were generated or analysed during the current study.

Declarations

Ethics approval and consent to participate

In this study, all animal experiments conducted strictly adhered to the guidelines set by the National Institutes of Health (NIH) and were officially approved by the Animal Ethics Committee of Wuhan University, with the ethical approval number ZN2023186. Furthermore, the experimental parts involving sepsis patients and healthy volunteers strictly followed the principles of the Declaration of Helsinki and were approved by the Medical Ethics Committee of Renmin Hospital, Wuhan University, with the ethical approval number WDRY2022-K046. Prior to inclusion in the study, written informed consent was obtained from all enrolled participants.

Competing interests

The authors declare no competing interests.

Author details

[1]Department of Anesthesiology, Research Centre of Anesthesiology and Critical Care Medicine, Zhongnan Hospital of Wuhan University, Wuhan, Hubei, China
[2]Department of Respiratory and Critical Care Medicine, Renmin Hospital of Wuhan University, Wuhan 430060, China
[3]Reproductive Medical Center, Renmin Hospital of Wuhan University, Wuhan, Hubei 430060, China

Received: 25 July 2024 / Accepted: 20 February 2025
Published online: 28 February 2025

References

1. Liu D, Huang SY, Sun JH, Zhang HC, Cai QL, Gao C, Li L, Cao J, Xu F, Zhou Y, et al. Sepsis-induced immunosuppression: mechanisms, diagnosis and current treatment options. Mil Med Res. 2022; 9:56.
2. Jiao Y, Zhang T, Zhang C, Ji H, Tong X, Xia R, Wang W, Ma Z, Shi X. Exosomal miR-30d-5p of neutrophils induces M1 macrophage polarization and primes macrophage pyroptosis in sepsis-related acute lung injury. Crit Care. 2021; 25:356.
3. Kwok AJ, Allcock A, Ferreira RC, Cano-Gamez E, Smee M, Burnham KL, Zurke YX, Emergency Medicine Research O, McKechnie S, Mentzer AJ, et al. Neutrophils and emergency granulopoiesis drive immune suppression and an extreme response endotype during sepsis. Nat Immunol. 2023; 24:767–779.
4. Zhang H, Wang Y, Qu M, Li W, Wu D, Cata JP, Miao C. Neutrophil, neutrophil extracellular traps and endothelial cell dysfunction in sepsis. Clin Transl Med. 2023; 13:e1170.
5. Wong SL, Wagner DD: Peptidylarginine deiminase 4. a nuclear button triggering neutrophil extracellular traps in inflammatory diseases and aging. Faseb j. 2018; 32:fj201800691R.
6. Huang J, Hong W, Wan M, Zheng L. Molecular mechanisms and therapeutic target of NETosis in diseases. MedComm. (2020) 2022; 3:e162.
7. Silva CMS, Wanderley CWS, Veras FP, Sonego F, Nascimento DC, Gonçalves AV, Martins TV, Cólon DF, Borges VF, Brauer VS, et al. Gasdermin D inhibition prevents multiple organ dysfunction during sepsis by blocking NET formation. Blood. 2021; 138:2702–2713.
8. Su Y, Yin X, Huang X, Guo Q, Ma M, Guo L. Astragaloside IV ameliorates sepsis-induced myocardial dysfunction by regulating NOX4/JNK/BAX pathway. Life Sci. 2022; 310:121123.
9. Xu J, Zhang Z, Ren D, Liu L, Xing H, Wang D, Wu Y, Zhang Y, Chen Q, Wang T. Astragaloside IV negatively regulates Gpr97-TPL2 signaling to protect against hyperhomocysteine-exacerbated sepsis associated acute kidney injury. Phytomedicine. 2024; 125:155346.
10. Sun Y, Ma Y, Sun F, Feng W, Ye H, Tian T, Lei M. Astragaloside IV attenuates lipopolysaccharide induced liver injury by modulating Nrf2-mediated oxidative stress and NLRP3-mediated inflammation. Heliyon. 2023; 9:e15436.
11. Dai H, Zheng Y, Chen R, Wang Y, Zhong Y, Zhou C, Zhan C, Luo J. Astragaloside IV alleviates sepsis-induced muscle atrophy by inhibiting the TGF-β1/Smad signaling pathway. Int Immunopharmacol. 2023; 115:109640.
12. Huang X, Zhang MZ, Liu B, Ma SY, Yin X, Guo LH. Astragaloside IV Attenuates Polymicrobial Sepsis-Induced Cardiac Dysfunction in Rats via IKK/NF-κB Pathway. Chin J Integr Med. 2021; 27:825–831.
13. Wei JY, Hu MY, Chen XQ, Wei JS, Chen J, Qin XK, Lei FY, Zou JS, Zhu SQ, Qin YH. Hypobaric Hypoxia Aggravates Renal Injury by Inducing the Formation of Neutrophil Extracellular Traps through the NF-κB Signaling Pathway. Curr Med Sci. 2023; 43:469–477.
14. Li Z, Hu E, Zheng F, Wang S, Zhang W, Luo J, Tang T, Huang Q, Wang Y. The effects of astragaloside IV on gut microbiota and serum metabolism in a mice model of intracerebral hemorrhage. Phytomedicine. 2023; 121:155086.
15. Song L, Zhang W, Tang SY, Luo SM, Xiong PY, Liu JY, Hu HC, Chen YQ, Jia B, Yan QH, et al. Natural products in traditional Chinese medicine: molecular mechanisms and therapeutic targets of renal fibrosis and state-of-the-art drug delivery systems. Biomed Pharmacother. 2024; 170:116039.
16. Liu J, Zhang Z, Dong J, Chen A, Qiu J, Li C. Electrochemical immunosensor based on hollow Pt@Cu(2)O as a signal label for dual-mode detection of procalcitonin. Talanta. 2024; 266:125018.
17. Zhou R, You Y, Zha Z, Chen J, Li Y, Chen X, Chen X, Jiang X, Chen J, Kwan HY, et al. Biotin decorated celastrol-loaded ZIF-8 nano-drug delivery system targeted epithelial ovarian cancer therapy. Biomed Pharmacother. 2023; 167:115573.
18. Bai Y, Min R, Chen P, Mei S, Deng F, Zheng Z, Jiang C, Miao R, Wu Z, Zhang P, et al. Disulfiram blocks inflammatory TLR4 signaling by targeting MD-2. Proc Natl Acad Sci U S A. 2023; 120:e2306399120.
19. Murray GI, Barnes TS, Sewell HF, Ewen SW, Melvin WT, Shaw PM, Fowler J, Burke MD. Cytochrome P-450 localization in normal human adult and foetal liver by immunocytochemistry using a monoclonal antibody against human cytochrome P-450. Histochem J. 1987; 19:537–545.
20. Zhu CL, Wang Y, Liu Q, Li HR, Yu CM, Li P, Deng XM, Wang JF. Dysregulation of neutrophil death in sepsis. Front Immunol 2022; 13:963955.
21. Li Z, Feng Y, Zhang S, Li T, Li H, Wang D, Hao K, He C, Tian H, Chen X. A Multifunctional Nanoparticle Mitigating Cytokine Storm by Scavenging Multiple Inflammatory Mediators of Sepsis. ACS Nano. 2023; 17:8551–8563.
22. Ou Q, Tan L, Shao Y, Lei F, Huang W, Yang N, Qu Y, Cao Z, Niu L, Liu Y, et al. Electrostatic Charge-Mediated Apoptotic Vesicle Biodistribution Attenuates Sepsis by Switching Neutrophil NETosis to Apoptosis. Small. 2022; 18:e2200306.
23. Thiam HR, Wong SL, Qiu R, Kittisopikul M, Vahabikashi A, Goldman AE, Goldman RD, Wagner DD, Waterman CM. NETosis proceeds by cytoskeleton and endomembrane disassembly and PAD4-mediated chromatin decondensation and nuclear envelope rupture. Proc Natl Acad Sci U S A. 2020; 117:7326–7337.
24. Sun B, Dwivedi N, Bechtel TJ, Paulsen JL, Muth A, Bawadekar M, Li G, Thompson PR, Shelef MA, Schiffer CA, et al. Citrullination of NF-κB p65 promotes its nuclear localization and TLR-induced expression of IL-1β and TNFα. Sci Immunol. 2017; 2.
25. Chen J, Wang T, Li X, Gao L, Wang K, Cheng M, Zeng Z, Chen L, Shen Y, Wen F; DNA of neutrophil extracellular traps promote NF-κB-dependent autoimmunity via cGAS/TLR9 in chronic obstructive pulmonary disease. Signal Transduct Target Ther. 2024; 9:163.
26. Yu Y, Koehn CD, Yue Y, Li S, Thiele GM, Hearth-Holmes MP, Mikuls TR, O'Dell JR, Klassen LW, Zhang Z, Su K. Celastrol inhibits inflammatory stimuli-induced neutrophil extracellular trap formation. Curr Mol Med. 2015; 15:401–410.
27. Ju M, Liu B, He H, Gu Z, Liu Y, Su Y, Zhu D, Cang J, Luo Z. MicroRNA-27a alleviates LPS-induced acute lung injury in mice via inhibiting inflammation and apoptosis through modulating TLR4/MyD88/NF-κB pathway. Cell Cycle. 2018; 17:2001–2018.

28. Silva-Gomez JA, Galicia-Moreno M, Sandoval-Rodriguez A, Miranda-Roblero HO, Lucano-Landeros S, Santos A, Monroy-Ramirez HC, Armendariz-Borunda J. Hepatocarcinogenesis Prevention by Pirfenidone Is PPARγ Mediated and Involves Modification of Nuclear NF-kB p65/p50 Ratio. Int J Mol Sci. 2021; 22.
29. Zhu R, Zheng J, Chen L, Gu B, Huang S. Astragaloside IV facilitates glucose transport in C2C12 myotubes through the IRS1/AKT pathway and suppresses the palmitate-induced activation of the IKK/IκBα pathway. Int J Mol Med. 2016; 37:1697–1705.
30. Chu C, Wang X, Yang C, Chen F, Shi L, Xu W, Wang K, Liu B, Wang C, Sun D, Ding W. Neutrophil extracellular traps drive intestinal microvascular endothelial ferroptosis by impairing Fundc1-dependent mitophagy. Redox Biol. 2023; 67:102906.
31. Chen L, Zhao Y, Lai D, Zhang P, Yang Y, Li Y, Fei K, Jiang G, Fan J. Neutrophil extracellular traps promote macrophage pyroptosis in sepsis. Cell Death Dis. 2018; 9:597.
32. Carmona-Rivera C, Zhao W, Yalavarthi S, Kaplan MJ. Neutrophil extracellular traps induce endothelial dysfunction in systemic lupus erythematosus through the activation of matrix metalloproteinase-2. Ann Rheum Dis. 2015; 74:1417–1424.
33. Boufenzer A, Carrasco K, Jolly L, Brustolin B, Di-Pillo E, Derive M, Gibot S. Potentiation of NETs release is novel characteristic of TREM-1 activation and the pharmacological inhibition of TREM-1 could prevent from the deleterious consequences of NETs release in sepsis. Cell Mol Immunol. 2021; 18:452–460.

Publisher's note